

Nucleon form factors on a large volume lattice near the physical point in 2+1 flavor QCD

Ken-Ichi Ishikawa,^{1,2} Yoshinobu Kuramashi,^{3,2,*} Shoichi Sasaki,^{4,2,†}
Natsuki Tsukamoto,⁴ Akira Ukawa,^{5,2} and Takeshi Yamazaki^{6,3,2,‡}

(PACS Collaboration)

¹*Graduate School of Science, Hiroshima University, Higashi-Hiroshima, Hiroshima 739-8526, Japan*

²*RIKEN Advanced Institute for Computational Science, Kobe, Hyogo 650-0047, Japan*[§]

³*Center for Computational Sciences, University of Tsukuba, Tsukuba, Ibaraki 305-8577, Japan*

⁴*Department of Physics, Tohoku University, Sendai 980-8578, Japan*

⁵*Center for World Premier International Research Center Initiative (WPI),*

Japan Society for the Promotion of Science, Tokyo 102-0083, Japan

⁶*Faculty of Pure and Applied Sciences, University of Tsukuba, Tsukuba, Ibaraki, 305-8571, Japan*

(Dated: October 19, 2018)

We present results for the isovector nucleon form factors measured on a 96^4 lattice at almost the physical pion mass with a lattice spacing of 0.085 fm in 2+1 flavor QCD. The configurations are generated with the stout-smearred $O(a)$ -improved Wilson quark action and the Iwasaki gauge action at $\beta=1.82$. The pion mass at the simulation point is about 146 MeV. A large spatial volume of $(8.1 \text{ fm})^3$ allows us to investigate the form factors in the small momentum transfer region. We determine the isovector electric radius and magnetic moment from nucleon electric (G_E) and magnetic (G_M) form factors as well as the axial-vector coupling g_A . We also report on the results of the axial-vector (F_A), induced pseudoscalar (F_P) and pseudoscalar (G_P) form factors in order to verify the axial Ward-Takahashi identity in terms of the nucleon matrix elements, which may be called as the generalized Goldberger-Treiman relation.

I. INTRODUCTION

The nucleon vector and axial elastic form factors are good probes to investigate the internal structure of the nucleon [1]. Although great theoretical and experimental efforts have been devoted to improving our knowledge of the nucleon structure, there are several unsolved problems associated with fundamental properties of the proton and neutron. The proton radius puzzle, where high-precision measurements of the proton's electric charge radius from the muonic hydrogen Lamb shift [2, 3] disagree with well established results of both electron-proton scattering and hydrogen spectroscopy [4], is currently one of the most intriguing problems in this field [5]. The neutron lifetime puzzle, where the discrepancy between the results of beam experiments and storage experiments remains unsolved, is another open question that deserves further investigation in terms of the nucleon axial-vector coupling g_A [6].

Much effort has been devoted to calculating the nucleon form factors with lattice QCD since 1980's. Unfortunately, satisfactory results, that are consistent with the experiments, have not yet been achieved for the nucleon structure in the previous lattice QCD simulations. The current situation is that we are still struggling to reproduce well-known experimental results, *e.g.*, the axial-vector coupling and the electric charge radius. This means that we have not yet achieved our final goal of properly generating a single-nucleon state is properly generated in lattice QCD calculations. The discrepancy between existing lattice calculations and experimental values could be attributed to unresolved systematic er-

rors in numerical simulations. An important source of systematic uncertainty should be due to the fact that the simulated quark mass used in simulations is heavier than the physical one. However, the particular quantities like the axial-vector coupling [65] and the electric charge radius still show some discrepancies with respect to the experimental values in the previous lattice QCD simulations near the physical point [8–12].

In this paper, we aim to calculate the nucleon form factors in a very large spatial volume in realistic lattice QCD, where the light quark masses are down to their physical values. For this purpose, we use the 2+1 flavor QCD gauge configurations generated on a $(8.1 \text{ fm})^4$ lattice near the physical point (the pion mass m_π at the simulation point is about 146 MeV) by the PACS Collaboration [13]. There are three reasons for paying special attention to its large spatial volume of $(8.1 \text{ fm})^3$.

First of all, the large finite volume effect, represented by the $m_\pi L$ scaling (L denotes the spatial extent of the lattice volume), on measurements of the axial-vector coupling g_A was reported in Refs. [14, 15]. According to their conclusion, one can estimate that spatial sizes of 7.7–9.4 fm ($m_\pi L \approx 5.7 - 7.0$) for $m_\pi \approx 146$ MeV are necessary for keeping the finite volume effect on g_A at or below 1% [66].

Second, thanks to the large spatial volume, we can access to the small momentum transfer region up to 152 MeV. The momentum squared (q^2) dependence of the nucleon form factors can be carefully examined in the very large spatial volume. Indeed, the values of a given form factor at very low q^2 help to more accurately determine the slope of the form factor at $q^2 = 0$, which is associated with the root-mean-square (RMS) radius R .

In this context, uncertainties in the determination of R are sensitive to the size of the spatial extent L in physical units. For the case of the electric form factor (G_E), R corresponds to the charge radius.

Finally we revisit the recent claim in the literature that the charge density of the proton, which has the shape of an exponential in a classical argument, is widely distributed in space [5]. The q^2 dependence of the Sachs form factors $G_E(q^2)$ and $G_M(q^2)$ are roughly described by the dipole shape: $G_D(q^2) = \Lambda^2/(q^2 + \Lambda^2)^2$ with a single parameter Λ called the dipole mass parameter around 0.84 GeV [1]. The dipole form assumes that the spatial charge distribution is falling exponentially at large r as $\rho(r) \propto e^{-r\Lambda}$ [1]. For the sake of simplicity, we adopt the spatial charge distribution as $\rho(r) = \rho_0 e^{-r\Lambda}$, where ρ_0 is determined by the normalization condition. The RMS radius R is defined in terms of the charge density as

$$R^2 \equiv 4\pi \int_0^\infty \rho(r) r^4 dr, \quad (1)$$

which gives a relation of $R = \sqrt{12}/\Lambda$. We next introduce the truncated RMS radius $R(r_{\text{cut}})$, where the integral (1) is stopped at $r = r_{\text{cut}}$, and then calculate the following ratio as a function of r_{cut} [5]:

$$\frac{R(r_{\text{cut}})}{R} = \sqrt{1 - e^{-X} \left[1 + X + \frac{1}{2}X^2 + \frac{1}{6}X^3 + \frac{1}{24}X^4 \right]}, \quad (2)$$

where $X = r_{\text{cut}}\Lambda = \sqrt{12}r_{\text{cut}}/R$. To get more than 98% of R , the value of r_{cut} must be greater than $2.75R$, which is remarkably large value [5]. If we take it seriously, this intuitive argument suggests that the spatial extent of $2.75R \times 4$ [67], which is roughly 10 fm, is required for precise determination of the proton charge radius within a few-percent accuracy on a *periodic* hyper-cubic lattice.

This paper is organized as follows: In Sec. II, we present a brief introduction of general features of nucleon form factors. In Sec. III, we first summarize simulation parameters in 2+1 flavor ensembles generated by the PACS Collaboration [13] and then give some basic results from the nucleon two-point function. We also describe the lattice method (standard ratio method) for calculating the isovector form factors of the nucleon from relevant three-point correlation functions. The results of our lattice calculations for the nucleon form factors are presented in Sec. IV, which is divided into three major subsections. We first determine four kinds of nucleon couplings — the vector coupling g_V , the axial-vector coupling g_A , the scalar coupling g_S and the tensor coupling g_T — which are directly accessible from the three-point correlations function at zero momentum transfer in Sec. IV A. Section IV B presents the results of the isovector electric (G_E) and magnetic (G_M) form factors, including a detailed study of the momentum transfer dependence and determination of the isovector electric and magnetic RMS radii and also the isovector magnetic moment. The last subsection (Sec. IV C) is devoted to a

discussion of the results of three form factors obtained in the axial-vector and pseudoscalar channels, which are related by the axial Ward-Takahashi identity in terms of the nucleon matrix elements. Finally, we close with a brief summary and our conclusions in Sec. V.

II. GENERAL FEATURES OF NUCLEON FORM FACTORS

In general, four form factors appear in the nucleon matrix elements of the weak current. Here, for example, we consider the matrix element for neutron beta decay. In this case, the vector and axial-vector currents are given by $V_\alpha^+(x) = \bar{u}(x)\gamma_\alpha d(x)$ and $A_\alpha^+(x) = \bar{u}(x)\gamma_\alpha\gamma_5 d(x)$, and then the general form of the matrix element for neutron beta decay is expressed by both the vector and axial-vector transitions:

$$\langle p|V_\alpha^+(x) + A_\alpha^+(x)|n\rangle = \bar{u}_p (\mathcal{O}_\alpha^V(q) + \mathcal{O}_\alpha^A(q)) u_n e^{iq \cdot x}, \quad (3)$$

where $q = P_n - P_p$ is the momentum transfer between the neutron (n) and proton (p). The vector (F_V) and induced tensor (F_T) form factors are introduced for the vector matrix element,

$$\mathcal{O}_\alpha^V(q) = \gamma_\alpha F_V(q^2) + \sigma_{\alpha\beta} q_\beta F_T(q^2) \quad (4)$$

as well as the axial vector (F_A) and induced pseudoscalar (F_P) form factors for the axial-vector matrix element,

$$\mathcal{O}_\alpha^A(q) = \gamma_\alpha\gamma_5 F_A(q^2) + i q_\alpha\gamma_5 F_P(q^2). \quad (5)$$

These matrix elements are given here in the Euclidean metric convention (we have defined $\sigma_{\alpha\beta} = \frac{1}{2i}[\gamma_\alpha, \gamma_\beta]$) [68]. Thus, q^2 denoted in this paper, which stands for the Euclidean four-momentum squared, corresponds to the spacelike momentum squared as $q_M^2 = -q^2 < 0$ in Minkowski space.

The vector part of weak processes is related to the nucleon's electromagnetic matrix element through an isospin rotation if heavy-flavor contributions are ignored *under the exact isospin symmetry*. A simple exercise in $SU(2)$ Lie algebra leads to the following relation between the vector part of the weak matrix elements of neutron beta decay and the difference of proton and neutron electromagnetic matrix elements

$$\langle p|\bar{u}\gamma_\alpha d|n\rangle = \langle p|\bar{u}\gamma_\alpha u - \bar{d}\gamma_\alpha d|p\rangle \quad (6)$$

$$= \langle p|j_\alpha^{\text{em}}|p\rangle - \langle n|j_\alpha^{\text{em}}|n\rangle \quad (7)$$

where $j_\alpha^{\text{em}} = \frac{2}{3}\bar{u}\gamma_\alpha u - \frac{1}{3}\bar{d}\gamma_\alpha d$. Therefore, this relation gives a connection between the weak vector and induced tensor form factors and the *isovector* part of electromagnetic nucleon form factors

$$F_1^v(q^2) = F_V(q^2), \quad (8)$$

$$F_2^v(q^2) = 2M_N F_T(q^2), \quad (9)$$

where M_N denotes the nucleon mass, which is defined as the average of the neutron and proton masses. F_1^v (F_2^v)

TABLE I. Summary of simulation parameters in 2+1 flavor QCD simulations. See Ref. [13] for further details.

β	$L^3 \times T$	C_{SW}	κ_{ud}	κ_s	a [fm]	a^{-1} [GeV]	$(La)^3$	m_π [MeV]	N_{conf}
1.82	$96^3 \times 96$	1.11	0.126117	0.124790	0.0846(7)	2.333(18)	$\sim (8.1 \text{ fm})^3$	≈ 146	200

TABLE II. Choices for nonzero spatial momenta: $\mathbf{q} = \pi/48 \times \mathbf{n}$. The bottom row denote the degeneracy of \mathbf{n} due to the permutation symmetry between $\pm x, \pm y, \pm z$ directions.

label	Q0	Q1	Q2	Q3	Q4	Q5	Q6	Q7	Q8	Q9
\mathbf{n}	(0,0,0)	(1,0,0)	(1,1,0)	(1,1,1)	(2,0,0)	(2,1,0)	(2,1,1)	(2,2,0)	(3,0,0)	(2,2,1)
$ \mathbf{n} ^2$	0	1	2	3	4	5	6	8	9	9
degeneracy	1	6	12	8	6	24	24	12	6	24

is given by the *isovector* combination of the Dirac (Pauli) form factors of the proton and neutron as

$$F_{1,2}^v(q^2) = F_{1,2}^p(q^2) - F_{1,2}^n(q^2), \quad (10)$$

where individual form factors $F_{1,2}^N$ ($N = p, n$) are defined by

$$\begin{aligned} & \langle N(P') | j_\alpha^{\text{em}}(x) | N(P) \rangle \\ &= \bar{u}_N(P') \left(\gamma_\alpha F_1^N(q^2) + \sigma_{\alpha\beta} \frac{q_\beta}{2M_N} F_2^N(q^2) \right) u_N(P) e^{iq \cdot x}. \end{aligned} \quad (11)$$

Experimental data from elastic electron-nucleon scattering is usually described in terms of the electric $G_E(q^2)$ and magnetic $G_M(q^2)$ Sachs form factors, which are related to the Dirac and Pauli form factors:

$$G_E^N(q^2) = F_1^N(q^2) - \frac{q^2}{4M_N^2} F_2^N(q^2), \quad (12)$$

$$G_M^N(q^2) = F_1^N(q^2) + F_2^N(q^2). \quad (13)$$

Their normalizations at $q^2 = 0$ are given by the proton's (neutron's) electric charge and magnetic moment [69]. Therefore, one finds

$$\begin{aligned} F_V(0) &= F_1^v(0) = G_E^v(0) = 1, \\ 2M_N F_T(0) &= F_2^v(0) = G_M^v(0) - 1 = 3.70589, \end{aligned} \quad (14)$$

where G_E^v (G_M^v) represents the *isovector* combination of the electric (magnetic) form factors of the proton and neutron.

Regarding the q^2 dependence of the Sachs form factors $G_E^N(q^2)$ and $G_M^N(q^2)$, it is known experimentally that the standard dipole parametrization $G_D(q^2) = \Lambda^2/(\Lambda^2 + q^2)^2$ with $\Lambda^2 = 0.71$ [(GeV)²] (or $\Lambda = 0.84$ [GeV]) describes well the magnetic form factors of both the proton and neutron and also the electric form factor of the proton, at least, in the low q^2 region. In general, if there is no singularity around $q^2 = 0$ for a given form factor $G(q^2)$,

the normalized form factor can be expanded in powers of q^2 .

$$G(q^2) = G(0) \left(1 - \frac{1}{6} \langle r^2 \rangle q^2 + \frac{1}{120} \langle r^4 \rangle q^4 + \dots \right), \quad (16)$$

where the first coefficient determines the mean squared radius $\langle r^2 \rangle$, which is a typical size in the coordinate space. For the dipole form, the root-mean-square (RMS) radius R is given as $R = \sqrt{\langle r^2 \rangle} = \frac{\sqrt{12}}{\Lambda}$ by the dipole mass parameter Λ .

For the axial-vector part of weak processes, the axial-vector form factor at zero momentum transfer, namely, the axial-vector coupling $g_A = F_A(0)$, is precisely determined by measurements of the beta asymmetry in neutron decay. The value of $g_A = 1.2724(23)$ was quoted in the 2018 PDG [4]. The reason why g_A deviates from the corresponding vector coupling $g_V = F_V(0) = 1$ is that the axial-vector current is strongly affected by the spontaneous chiral symmetry breaking in the strong interaction [17, 18]. In this sense, this particular quantity allows us to perform a precision test of lattice QCD in the baryon sector.

The q^2 dependence of the axial-vector form factor $F_A(q^2)$ has also been studied in experiments, where the dipole form $F_A(q^2) = F_A(0)/(q^2 + M_A^2)^2$ is a good description for low and moderate momentum transfer $q^2 < 1$ [(GeV)²] [19, 20]. Recently, the axial mass parameter M_A has received much attention in neutrino oscillation studies [21, 22].

Although the induced pseudoscalar form factor $F_P(q^2)$ is less well known experimentally [23, 24], it is theoretically known that two form factors $F_A(q^2)$ and $F_P(q^2)$ in the axial-vector channel are not fully independent. It is because the axial Ward-Takahashi identity: $\partial_\alpha A_\alpha^+(x) = 2\hat{m}P^+(x)$ leads to the generalized Goldberger-Treiman (GT) relation among three form factors [25, 26]:

$$2M_N F_A(q^2) - q^2 F_P(q^2) = 2\hat{m} G_P(q^2), \quad (17)$$

where $\hat{m} = m_u = m_d$ is a degenerate up and down quark mass and the pseudoscalar nucleon form factor $G_P(q^2)$ is

defined in the pseudoscalar nucleon matrix element

$$\langle p|P^+(x)|n\rangle = \bar{u}_p(\gamma_5 G_P(q^2)) u_n e^{iq \cdot x} \quad (18)$$

with a local pseudoscalar density, $P^+(x) \equiv \bar{u}(x)\gamma_5 d(x)$. Therefore, the q^2 dependences of three form factors, $F_A(q^2)$, $F_P(q^2)$ and $G_P(q^2)$ are constrained by Eq. (17) as a consequence of the axial Ward-Takahashi identity. Therefore, the three form factors, $F_A(q^2)$, $F_P(q^2)$ and $G_P(q^2)$ are very important for verifying the axial Ward-Takahashi identity in terms of the nucleon matrix elements.

The latest lattice calculations of the nucleon structure have been carried out with increasing accuracy [7–12, 14–16, 27–30]. It seems that there is still a gap between experimentally known values and the lattice results, especially for the electric-magnetic nucleon radii and the magnetic moment. Our preliminary results computed near the physical pion mass in very large volume show agreement with experimental results [31–33]. In this paper, we present an update of our previous studies [31–33], including the axial-vector, induced pseudoscalar and pseudoscalar form factors.

TABLE III. Fitted energies of the nucleon state with the ten lowest momenta obtained from the smear-local case of the nucleon two-point function. Results for the nucleon energies $E_N(\mathbf{n}^2)$ with nonzero momenta are averaged over all possible permutations of $\mathbf{n} = (n_x, n_y, n_z)$, including both positive and negative directions. The values of the corresponding momentum squared $q^2 = 2M_N(E_N - M_N)$ are also tabulated.

label	$aE_N(\mathbf{n})$ (Smear-Local)	fit range	q^2 [(GeV) ²]
Q0	0.4107(12)	[8:15]	0
Q1	0.4161(12)	[8:15]	0.024(1)
Q2	0.4215(12)	[8:15]	0.048(2)
Q3	0.4268(13)	[8:15]	0.072(2)
Q4	0.4320(13)	[8:15]	0.095(3)
Q5	0.4373(14)	[8:15]	0.119(4)
Q6	0.4427(15)	[8:15]	0.143(5)
Q7	0.4531(18)	[8:15]	0.189(7)
Q8	0.4575(21)	[8:15]	0.209(8)
Q9	0.4588(20)	[8:15]	0.215(8)

III. SIMULATION DETAILS

We use the 2+1 flavor QCD gauge configurations generated with the 6-APE stout-smear $O(a)$ -improved Wilson-clover quark action and the Iwasaki gauge action [34] on a lattice $L^3 \times T = 96^3 \times 96$ at $\beta = 1.82$, which corresponds to a lattice cutoff of $a^{-1} \approx 2.3$ GeV ($a \approx 0.085$ fm) [13]. Periodic boundary conditions are used for the gauge and quark fields in all four directions. The stout smearing parameter is set to $\rho = 0.1$ [35].

The improvement coefficient, $c_{\text{SW}} = 1.11$, is determined nonperturbatively using the Schrödinger functional (SF) scheme [36]. The improved factor c_A for the axial-vector current becomes very small at the nonperturbative value of c_{SW} and is consistent with zero within the statistical error [36]. Therefore, we do not consider $\mathcal{O}(a)$ improvement of the quark bilinear current. The hopping parameters for the light sea quarks $(\kappa_{ud}, \kappa_s) = (0.126117, 0.124790)$ are chosen to be near the physical point. For the first time, a simulated pion mass reaches down to $m_\pi \approx 146$ MeV in a large spatial volume of $(8.1 \text{ fm})^3$ in 2+1 flavor QCD. A brief summary of our simulation parameters with 2+1 flavor QCD simulations is given in Table I.

The degenerated up-down quarks are simulated with the DDHMC algorithm [37, 38] using the even-odd preconditioning and the twofold mass preconditioning [39, 40]. The strange quark is simulated with the UVPHMC algorithm [41–46] where the action is UV filtered [47, 48] after the even-odd preconditioning without domain decomposition. The total number of gauge configurations reaches 200 which corresponds to 2000 trajectories after thermalization. Each measurement is separated by 10 trajectories. The results for the hadron spectrum and other physical quantities were already presented in Ref. [13]. We use the jackknife method with a bin size of 50 trajectories to estimate the statistical errors. Our preliminary results of the nucleon vector form factors with less number of measurements were first reported in Refs. [31, 32].

A. Nucleon two-point functions

Let us first examine the nucleon rest mass and the dispersion relation, which are obtained from the nucleon two-point functions. In order to compute nucleon energies or matrix elements, we define the nucleon (proton) operator as

$$N_X(t, \mathbf{p}) = \sum_{\mathbf{x}, \mathbf{x}_1, \mathbf{x}_2, \mathbf{x}_3} e^{-i\mathbf{p} \cdot \mathbf{x}} \varepsilon_{abc} [u_a^T(\mathbf{x}_1, t) C \gamma_5 d_b(\mathbf{x}_2, t)] u_c(\mathbf{x}_3, t) \times \phi(\mathbf{x}_1 - \mathbf{x}) \phi(\mathbf{x}_2 - \mathbf{x}) \phi(\mathbf{x}_3 - \mathbf{x}), \quad (19)$$

where the superscript T denotes a transposition and C is the charge-conjugation matrix defined as $C = \gamma_4 \gamma_2$. The indices abc and ud label color and flavor, respectively. The subscript X of the nucleon operator specifies the type of the smearing for the quark propagators. In this study, we use two types of smearing function ϕ : the local function as $\phi(\mathbf{x}_i - \mathbf{x}) = \delta(\mathbf{x}_i - \mathbf{x})$ (denoted as $X = L$) and the exponential smearing function: $\phi(\mathbf{x}_i - \mathbf{x}) = A \exp[-B|\mathbf{x}_i - \mathbf{x}|]$ with $A = 1.2$ and $B = 0.11$ (denoted as $X = S$). For simplicity, $\mathbf{x}_1 = \mathbf{x}_2 = \mathbf{x}_3$ is chosen.

We then construct two types of two-point functions with the exponential smearing source (the source-time

location denoted as t_{src}) as

$$C_{XS}(t_{\text{sink}} - t_{\text{src}}, \mathbf{p}) = \frac{1}{4} \text{Tr} \{ \mathcal{P}_+ \langle N_X(t_{\text{sink}}, \mathbf{p}) \bar{N}_S(t_{\text{src}}, -\mathbf{p}) \rangle \}, \quad (20)$$

where $X = L$ (local) or S (smear) stands for the type of smearing at the sink operator (with the sink-time location denoted as t_{sink}). A projection operator $\mathcal{P}_+ = \frac{1+\gamma_4}{2}$ can eliminate contributions from the opposite-parity state for $|\mathbf{p}| = 0$ [49, 50]. In this study, for nonzero spatial momentum, we use the nine lowest momenta: $\mathbf{p} = 2\pi/L \times \mathbf{n}$ with the vector of integers $\mathbf{n} \in Z^3$. All choices of \mathbf{n} are listed in Table II.

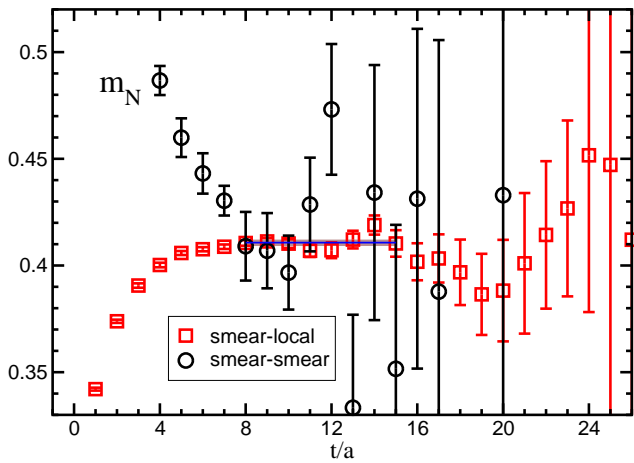


FIG. 1. Effective mass for the nucleon from the smear-local (squared symbols) and smear-smear (circle symbols) cases of the nucleon two-point functions.

B. Nucleon spectra and dispersion relation

In Fig. 1 we plot the nucleon effective mass with $|\mathbf{p}| = 0$ for two cases: smear-local denotes the nucleon two-point function with the smeared source and the local sink operators and smear-smear denotes the smeared source and the smeared sink ones. The values of the smearing parameters ($A = 1.2$ and $B = 0.11$) are chosen to optimize the effective mass plateau for the smear-local case. We thus observe that the smear-local case shows a good plateau for $t/a \geq 6$ with our choice of smearing parameters. On the other hand, the signal becomes noisier for the smear-smear case since the extra smearing in general causes statistical noise.

We also measure the nucleon energies $E_N(\mathbf{p})$ from the smear-local case of the nucleon two-point function for nine different cases with nonzero spatial momenta. All fit results for $E_N(\mathbf{p})$ obtained from the single-exponential

fit, where we take into account the full covariance matrix of the data during the fitting process, are tabulated in Table III.

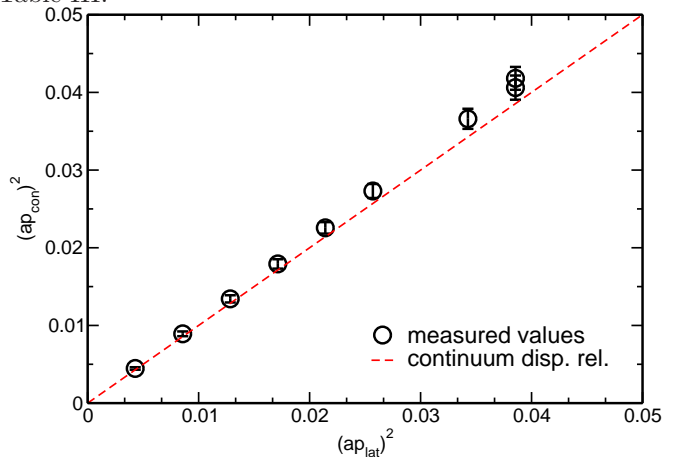


FIG. 2. Check of the dispersion relation for the nucleon. The variables p_{con}^2 and p_{lat}^2 appearing on the x-axis and y-axis are defined in the text. For comparison, the relativistic continuum dispersion relation is denoted as a dashed line.

Figure 2 shows a check of the dispersion relation for the nucleon. The vertical axis shows the momentum squared defined through the relativistic continuum dispersion relation as $p_{\text{con}}^2 = E_N^2(\mathbf{p}) - M_N^2$, while the horizontal axis shows the momentum squared given by the lattice momentum $p_{\text{lat}}^2 = (2\pi/L)^2 \times |\mathbf{n}|^2$ in lattice units. As can be seen in Fig. 2, the relativistic continuum dispersion relation is well satisfied up to $|\mathbf{n}|^2 = 9$.

C. Three-point correlation functions for nucleon form factors

The nucleon form factors are extracted from the three-point correlation functions consisting of the nucleon source and sink operators with a given local current J_α^O ($O = S, P, V, A$ and T) located at the time slice t :

$$C_{O,\alpha}^{P_k}(t, \mathbf{p}', \mathbf{p}) = \frac{1}{4} \text{Tr} \{ \mathcal{P}_k \langle N(t_{\text{sink}}, \mathbf{p}') J_\alpha^O(t, \mathbf{q}) \bar{N}(t_{\text{src}}, -\mathbf{p}) \rangle \}, \quad (21)$$

where \mathcal{P}_k denotes an appropriate projection operator to extract the form factors and $\mathbf{q} = \mathbf{p} - \mathbf{p}'$ represents the three-dimensional momentum transfer. The local current is given by $J_\alpha^O = \bar{u}(\Gamma^O)_\alpha d$ where Γ^O is a Dirac matrix appropriate for the channel O .

We then calculate the following ratio constructed from the three-point correlation function $C_{O,\alpha}^P$ with the nucleon two-point functions C_{XS} :

$$\mathcal{R}_{O,\alpha}^k(t, \mathbf{p}', \mathbf{p}) = \frac{C_{O,\alpha}^{\mathcal{P}_k}(t, \mathbf{p}', \mathbf{p})}{C_{SS}(t_{\text{sink}} - t_{\text{src}}, \mathbf{p}')} \sqrt{\frac{C_{LS}(t_{\text{sink}} - t, \mathbf{p}) C_{SS}(t - t_{\text{src}}, \mathbf{p}') C_{LS}(t_{\text{sink}} - t_{\text{src}}, \mathbf{p}')}{C_{LS}(t_{\text{sink}} - t, \mathbf{p}') C_{SS}(t - t_{\text{src}}, \mathbf{p}) C_{LS}(t_{\text{sink}} - t_{\text{src}}, \mathbf{p})}}, \quad (22)$$

which is a function of the current operator insertion time t at the given values of momenta \mathbf{p} and \mathbf{p}' for the initial and final states of the nucleon.

We consider only the rest frame of the final state with $\mathbf{p}' = \mathbf{0}$, which leads to $q^2 = 2M_N(E_N(\mathbf{q}) - M_N)$ for the squared four-momentum transfer. Hereafter, the nucleon energy $E_N(\mathbf{q})$ is simply abbreviated as E_N . In this kinematics, $\mathcal{R}_{O,\alpha}(t, \mathbf{p}', \mathbf{p})$ is represented by a simple notation $\mathcal{R}_{O,\alpha}(t, \mathbf{q})$. We calculate only the connected diagrams to concentrate on the *isovector* part of the nucleon form factors. The current insertion points t are moved between the nucleon source and sink operators, both of which are exponentially smeared in the Coulomb gauge, separated by 15 time slices. In the physical units, the source-sink separation of $t_{\text{sep}}/a = 15$ (denoted as $t_{\text{sep}} = t_{\text{sink}} - t_{\text{src}}$) corresponds to 1.27 fm. In previous calculations [11, 12, 15, 27, 28, 30], the maximum values of the source-sink separation were typically as large as 1.3-1.4 fm, where the excited-state effect is marginally insignificant.

The three-point correlation functions are calculated using the sequential source method with a fixed source location [51, 52]. This method requires the sequential quark propagator for each choice of a projection operator \mathcal{P} regardless of the types of current J_α^O . To minimize the numerical cost, we consider two types of the projection operators $\mathcal{P}_t = \mathcal{P}_{+\gamma_4}$ and $\mathcal{P}_{5z} = \mathcal{P}_{+\gamma_5\gamma_3}$ in this study.

The ratio (22) with appropriate combinations of the projection operator \mathcal{P}_k ($k = t, 5z$) and the α component of the current j_α^O gives the asymptotic values [26]:

$$\mathcal{R}_{V,4}^t(t, \mathbf{q}) \rightarrow \sqrt{\frac{E_N + M_N}{2E_N}} G_E^v(q^2) \quad (23)$$

and

$$\mathcal{R}_{V,i}^{5z}(t, \mathbf{q}) \rightarrow \frac{-i\varepsilon_{ij3}q_j}{\sqrt{2E_N(E_N + M_N)}} G_M^v(q^2) \quad (24)$$

for the vector current ($O = V$) in the limit when the Euclidean time separation between all operators is large, $t_{\text{sink}} \gg t \gg t_{\text{src}}$ with fixed t_{src} and t_{sink} . Similarly, we get

$$\begin{aligned} & \mathcal{R}_{A,i}^{5z}(t, \mathbf{q}) \\ & \rightarrow \sqrt{\frac{E_N + M_N}{2E_N}} \left[F_A(q^2) \delta_{i3} - \frac{q_i q_3}{E_N + M_N} F_P(q^2) \right] \end{aligned} \quad (25)$$

for the axial-vector current ($O = A$), and

$$\mathcal{R}_P^{5z}(t, \mathbf{q}) \rightarrow \frac{iq_3}{\sqrt{2E_N(E_N + M_N)}} G_P(q^2) \quad (26)$$

for the pseudoscalar ($O = P$), respectively. Here, we recall that the lattice operators receive finite renormalizations relative to their continuum counterparts in general. Thus, all of the above form factors G_E^v , G_M^v , F_A , F_P and G_P are not renormalized yet. Their renormalized values require the renormalization factor Z_O ($O = V, A, P$), which is defined through the renormalization of the quark bilinear currents

$$[\bar{u}\Gamma^O d]^{\text{ren}} = Z_O [\bar{u}\Gamma^O d]^{\text{lattice}}. \quad (27)$$

The renormalization factors Z_V , Z_A and Z_P are independently obtained using the SF scheme at the vanishing quark mass defined by the partially conserved axial-vector current (PCAC) relation [53]. Hereafter, the *isovector* electric G_E^v and magnetic G_M^v form factors are simply abbreviated as G_E and G_M .

IV. RESULTS OF NUCLEON FORM FACTORS

All the results presented in this work are obtained with 200 configurations. To reduce the statistical uncertainties, we perform 64 measurements of the two-point and three-point correlation functions on each configuration. For 64 measurements, we use eight different source locations, four choices for a temporal direction on a 96^4 lattice, and two choices of both forward and backward directions in time. In the analysis, all 64 sets of three-point correlation functions and nucleon two-point functions are folded together to create the single-correlation functions, respectively. It can reduce possible autocorrelation among measurements. The statistical errors are evaluated using the jackknife analysis with a bin size of five configurations.

We employ nine cases of spacial momentum transfer $\mathbf{q} = \pi/48 \times \mathbf{n}$ with $|\mathbf{n}|^2 \leq 9$ as described in Table II. The minimum momentum transfer is about 152 MeV, which is as small as the pion mass. A difference between the results for Q8 and Q9 cases could probe the possible lattice discretization error.

TABLE IV. Summary of bare couplings for the vector, axial vector, scalar and tensor.

g_V^{bare}	g_A^{bare}	g_S^{bare}	g_T^{bare}
1.0511(47)	1.205(78)	1.117(407)	0.985(55)

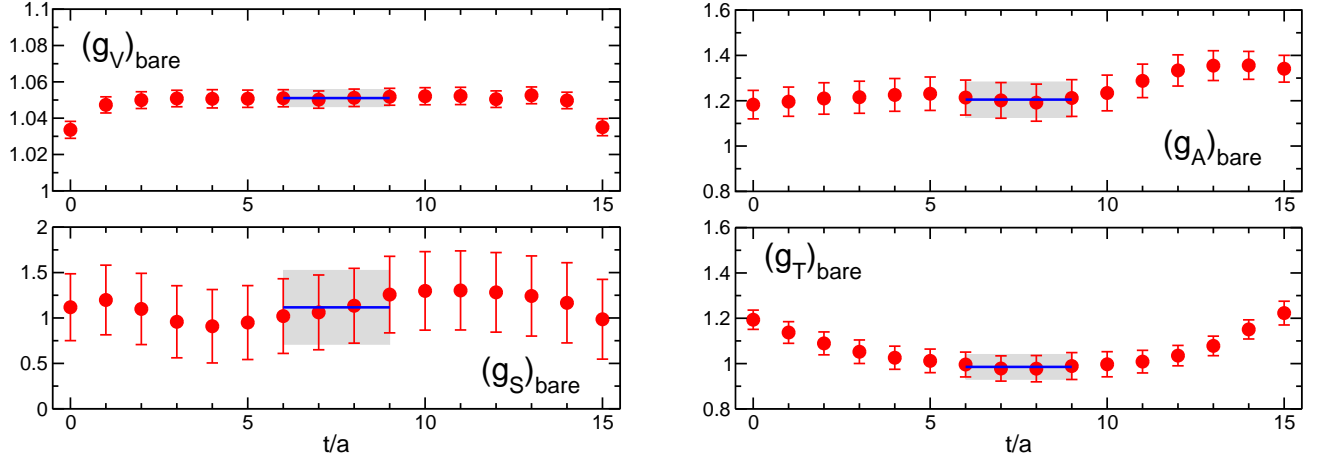


FIG. 3. Bare coupling g_O for $O = V$ (left upper), A (right upper), S (left lower) and T (right lower) as a function of the current insertion time slice.

A. Nucleon three-point function with zero momentum transfer

For zero momentum transfer $\mathbf{q} = \mathbf{0}$, the ratio (22) becomes

$$\mathcal{R}_{O,\alpha}^k(t, \mathbf{0}) = \frac{C_{O,\alpha}^{\mathcal{P}^k}(t, \mathbf{0})}{C_{SS}(t_{\text{sink}} - t_{\text{src}}, \mathbf{0})}, \quad (28)$$

which vanishes unless $\Gamma^O = 1(S), \gamma_4(V), \gamma_i \gamma_5(A)$, and $\sigma_{ij}(T)$ with $i, j = 1, 2, 3$ [52]. The nonvanishing ratio gives an asymptotic plateau corresponding to the bare value of the coupling g_O relevant for the O channel in the middle region between the source and sink points, when the condition $t_{\text{sink}} \gg t \gg t_{\text{src}}$ is satisfied.

With our choice of the projection operators $k = t, 5z$, we can determine four different couplings: the vector coupling g_V , the axial-vector coupling g_A , the scalar coupling g_S and the tensor coupling g_T , from the four ratios,

$$\mathcal{R}_{V,4}^t(t, \mathbf{0}) \rightarrow G_E(0) = F_V(0) = g_V, \quad (29)$$

$$\mathcal{R}_{A,3}^{5z}(t, \mathbf{0}) \rightarrow F_A(0) = g_A, \quad (30)$$

$$\mathcal{R}_S^t(t, \mathbf{0}) \rightarrow g_S, \quad (31)$$

$$\mathcal{R}_{T,12}^{5z}(t, \mathbf{0}) \rightarrow g_T, \quad (32)$$

whose values are not yet renormalized.

In Fig. 3, we plot the above four ratios as a function of the current insertion time slice t for the vector (left upper panel), axial-vector (right upper panel), scalar (left lower panel) and tensor (right lower panel) channels. The best plateau is clearly observed in the vector channel since the vector coupling g_V corresponds to the conserved charge associated to the isospin symmetry. The exact symmetry would suppress the statistical fluctuations and hinder parts of the excited-state contamination. Therefore, a very long plateau indeed appears in the ratio of $\mathcal{R}_{V,4}^t(t, \mathbf{0})$. It is also worth recalling that the time-reversal average was implemented in our averaging procedure on each configuration with multiple measurements, which

include both forward and backward propagations in time, as described previously.

In the vector channel (left upper panel), t dependence of $\mathcal{R}_{V,4}^t(t, \mathbf{0})$ is symmetric between the source ($t/a = 0$) and sink ($t/a = 15$) points. Although this symmetric behavior with respect to t is hindered by larger statistical fluctuations in both the scalar (left lower panel) and the axial-vector (right upper panel) channels, its behavior is clearly seen in the tensor channel (right lower panel) with relatively small errors. In the case of the tensor, good plateau is observed only in the middle region between the source and sink points. Therefore, we choose the range $6 \leq t/a \leq 9$, where an asymptotic plateau behavior appears in the ratio of $\mathcal{R}_{O,\alpha}^k(t, \mathbf{0})$ with our choice of source-sink separation.

In each plot, a solid line indicates the average value over range $6 \leq t/a \leq 9$ and a shaded band displays one standard deviation estimated using the jackknife method. The obtained values of the bare couplings g_O , which are not yet renormalized, are summarized in Table IV.

We next evaluate the renormalization factor of the local vector current Z_V through the property of $g_V^{\text{ren}} = 1$ for the renormalized value of the vector charge g_V^{ren} under the exact isospin symmetry. Therefore, the value of Z_V can be evaluated using $1/g_V^{\text{bare}}$ since $g_V^{\text{ren}} = Z_V g_V^{\text{bare}}$.

Figure 4 plots the result of Z_V , which shows a good plateau in the time range $2 \leq t/a \leq 14$. The constant-fit result with one-standard-error band denoted by three solid lines shows good consistency with the value of Z_V (red line) obtained using the SF scheme at the vanishing PCAC quark mass [53]. This consistency may suggest that the excited-state contamination in three-point functions is not serious with our choice of source-sink separation. We also draw the value of Z_A with the SF scheme for comparison in the same figure. The difference between Z_V and Z_A is 1.5%, which indicates a fairly small chiral symmetry breaking effect in our simulations.

The local axial-vector current is renormalized with

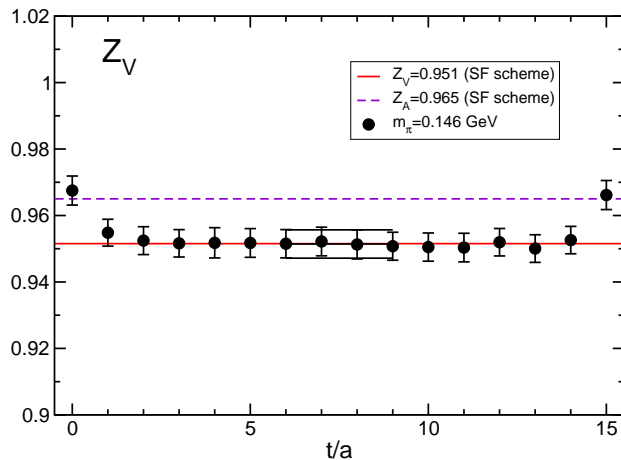


FIG. 4. Renormalization factor of the local vector current determined by $Z_V = 1/g_V^{\text{bare}}$.

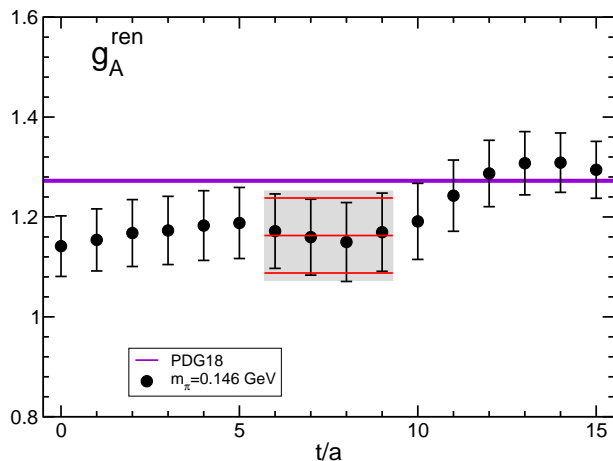


FIG. 5. Renormalized axial charge with $Z_A = 0.9650(68)(95)$ in the SF scheme.

the value of $Z_A = 0.9650(68)(95)$ obtained with the SF scheme [53] shown in Fig. 4. We then plot the renormalized value of the axial charge $g_A^{\text{ren}} = Z_A g_A^{\text{bare}}$ as a function of the current insertion time slice t in Fig. 5. The three solid lines represent the fit result with one-standard error band in the time region of $6 \leq t/a \leq 9$, while the uncertainty in the determination of the value of Z_A is taken into account by the shaded band. We finally obtain the renormalized value of the axial charge

$$g_A^{\text{ren}} = 1.163(75)_{\text{stat}}(14)_{Z_A}, \quad (33)$$

which slightly underestimates the experimental value of $1.2724(23)$ by less than 10%. However, the dominant statistical error is of the same order. We also recall that the t dependence of $\mathcal{R}_{A,3}^{5z}(t, \mathbf{0})$ in Fig. 3 shows large wiggles, which seem to break time reversal between the source and sink points. However the time-reversal feature should eventually be restored as observed in the vector and tensor channels. This suggests that the ratio of $\mathcal{R}_{A,3}^{5z}(t, \mathbf{0})$ still has large statistical fluctuations, which are not well

under control. A new class of statistical error reduction techniques such as low-eigenmode deflation and all-mode-averaging (AMA) [54] should be useful and efficient to improve the statistical accuracy of $\mathcal{R}_{A,3}^{5z}(t, \mathbf{0})$ with the limited number of configurations. We intend to examine this possibility in future research.

B. Results of nucleon form factors in the vector channel

1. Electric G_E and magnetic G_M form factors

The *isovector* electric form factor G_E and magnetic form factor G_M are separately obtained from the ratios (23) and (24). Figure 6 shows the ratios of the three- and two-point functions (23) and (24) as a function of the current insertion time slice t for the *isovector* electric form factor G_E (left) and magnetic form factor G_M (right) at the nine lowest nonzero momentum transfers after extracting the relevant kinematical factors. Although the time region $6 \leq t/a \leq 9$ certainly exhibits an asymptotic plateau at low momentum transfers with our choice of source-sink separation, the plateau region is not clearly defined at the higher momentum transfers especially for the magnetic form factor G_M .

This observation suggests that the excited-state contamination could not be well under control for the higher momentum transfers with the source-sink separation $t_{\text{sep}}/a = 15$, since our choice of source-sink separation is determined with a set of the smearing parameters ($A = 1.2$ and $B = 0.11$ for the exponential smearing function as described previously) that is optimized for the case of the nucleon operator with zero momentum. However, the remaining excited-state contamination is relatively smaller than the statistical uncertainties on both electric and magnetic form factors at the higher momentum transfers. Therefore, we simply evaluate the values of both G_E and G_M form factors by constant fits to the data points in the range $6 \leq t/a \leq 9$ denoted by the gray shaded area as in the cases of the coupling g_O ($O = V, A, S, T$).

In Table V, we compile the results for G_E and G_M form factors together with the results of F_1 and F_2 form factors, which are evaluated using linear combinations of G_E and G_M with appropriate coefficients determined by Eqs. (23) and (24) with measured values of the momentum squared q^2 and the nucleon mass M_N . The q^2 dependences of G_E (left panel) and G_M (right panel) are plotted in Fig. 7, respectively. For the finite three-momentum \mathbf{q} , we use the nine lowest nonzero momenta: $\mathbf{q} = \pi/48 \times \mathbf{n}$ with $|\mathbf{n}|^2 \leq 9$. The lowest nonzero momentum transfer q^2 in the present work reaches the value of $0.024(1) [(\text{GeV})^2]$, which is much smaller than $4m_\pi^2$ even at $m_\pi \approx 146$ MeV. In each panel, we also plot Kelly's fit [55] (red dashed curves) as their experimental data. The simulated electric form factor G_E is fairly consistent with the experimental results, especially at low q^2 . The

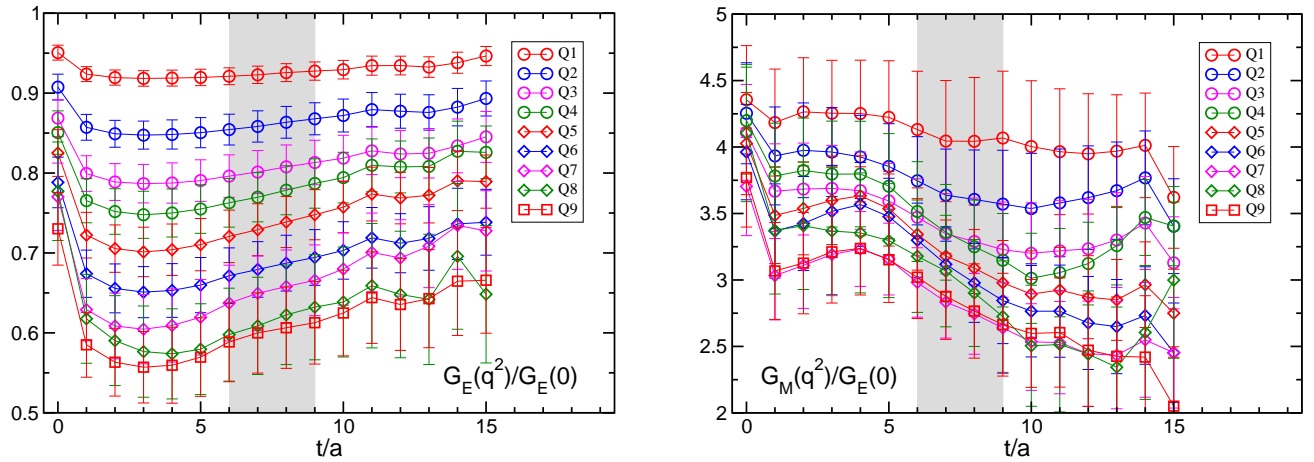


FIG. 6. Ratios of the three- and two-point functions (23) and (24) for the *isovector* electric form factor G_E (left) and magnetic form factor G_M (right) at the nine lowest nonzero momentum transfers after extracting the relevant kinematical factors. The gray shaded area ($6 \leq t/a \leq 9$) in each panel shows the region where the values of the corresponding form factor are estimated.

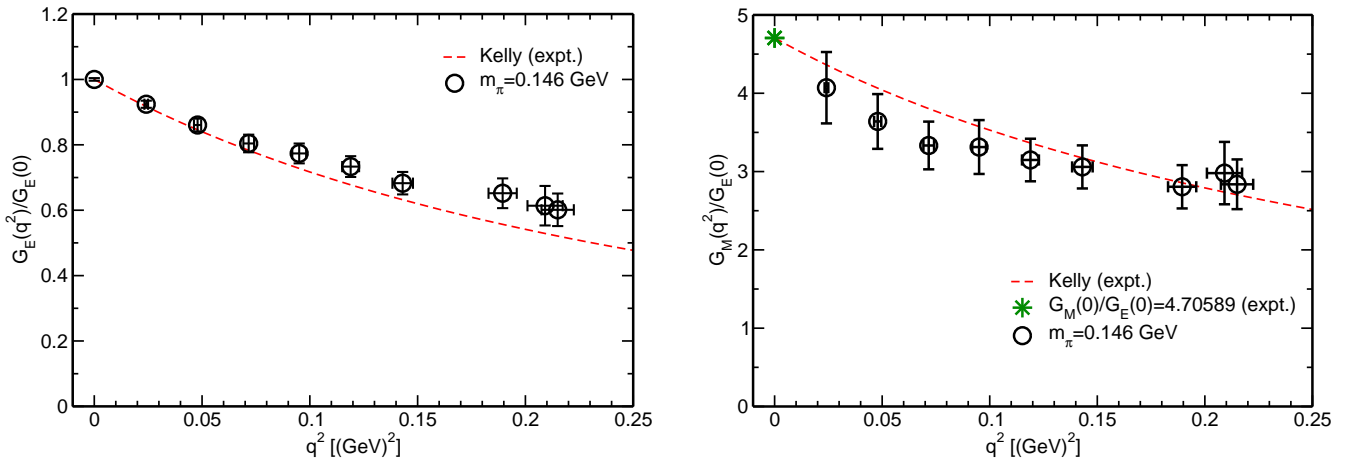


FIG. 7. Momentum-squared dependence of the *isovector* electric form factor G_E (left) and magnetic form factor G_M (right). We also plot Kelly's fit [55] as their experimental data.

magnetic form factor G_M agrees with Kelly's fit albeit with rather large errors.

This feature suggests that our results successfully reproduce the experimental value for the electric RMS radius. On the other hand, noisier signals for G_M would prevent the precise determination of the magnetic RMS radius. The electric (magnetic) RMS radius, $\sqrt{\langle r_E^2 \rangle}$ ($\sqrt{\langle r_M^2 \rangle}$), can be evaluated from the slope of the respective form factor at zero momentum transfer

$$\langle r_l^2 \rangle = - \frac{6}{G_l(0)} \left. \frac{dG_l(q^2)}{dq^2} \right|_{q^2=0} \quad (34)$$

with $l = E$ (M). Recall that G_M at zero momentum transfer, whose value corresponds to the isovector magnetic moment $\mu_v = G_M(0)$, cannot be directly measured for kinematical reasons [26]. Therefore, a q^2 -extrapolation is necessary to evaluate the value of $G_M(0)$.

In principle, low- q^2 data points are crucial for determining both the RMS radii and magnetic moment. How-

ever, the accessible momentum transfer is limited on the lattice since the components of the three momentum are discrete in units of $2\pi/L$. In this sense, a large spatial size L is required to precisely determine the RMS radii ($\sqrt{\langle r_E^2 \rangle}$ and $\sqrt{\langle r_M^2 \rangle}$) and magnetic moment (μ_v).

The determination of the slope (or q^2 extrapolation) is highly sensitive to how we fit the q^2 -dependence of the form factors. In the previous studies [11, 15, 27–29], the dipole form $G(q^2) = a_0/(1 + a_1 q^2)^2$, and the polynomial form $G(q^2) = \sum_{k=0} d_k q^{2k}$ were often adopted for G_E and G_M . However, the fitting form ansatz may tend to constrain an interpolation (or extrapolation) and introduce a model dependence into the final result for the RMS radius (or the value of $G(0)$). In order to reduce systematic errors associated with the interpolation or extrapolation of the form factor in momentum transfer, we use the model-independent z -expansion method [56, 57].

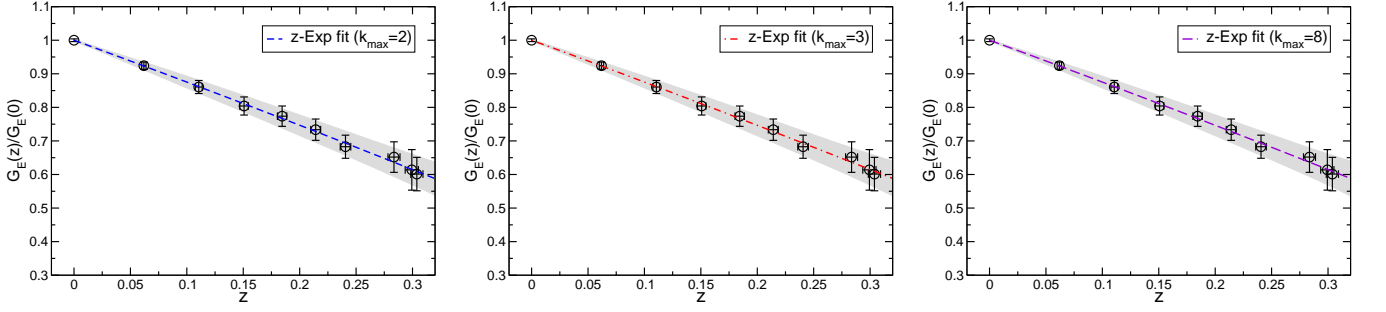


FIG. 8. Results for z -Exp fit of G_E with $k_{\max} = 2$ (left), 3 (middle) and 8 (right) using all ten data points.

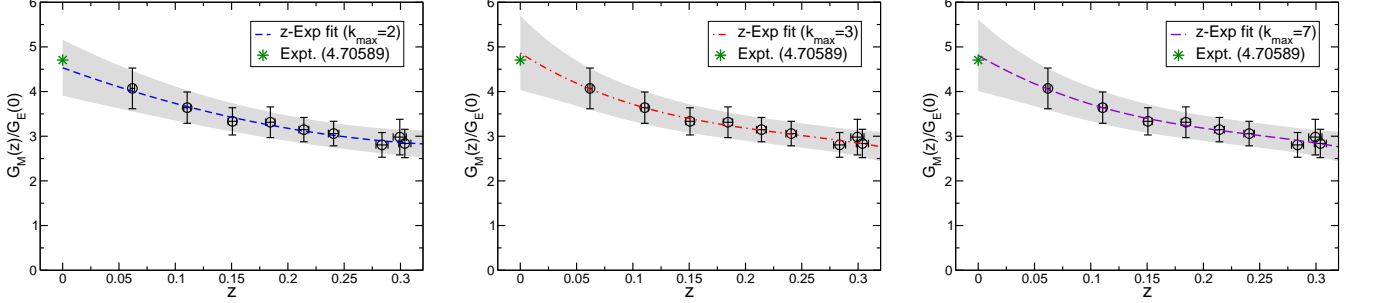


FIG. 9. Results for the z -Exp fit of G_M with $k_{\max} = 2$ (left), 3 (middle) and 7 (right) using all nine data points.

2. Analysis with z -expansion method

Let us recall the analytic structure of the form factors in the complex q^2 plane. There is a nonanalytic region for $G(q^2)$ due to threshold of two or more particles, *e.g.* the 2π continuum. Hence the q^2 expansion, $G(q^2) = \sum_{k=0} d_k q^{2k}$, does not converge if $|q^2| > 4m_\pi^2$ where $q^2 = -4m_\pi^2$ is a branch point associated with the pion pair creation for $G = G_E$ or G_M [57].

The z -expansion (denoted as z -Exp) makes use of a conformal mapping from q^2 to a new variable z . Since this transformation maps the analytic domain mapped inside a unit-circle $|z| < 1$ in the z -plane, the form factors

can be described by a convergent Taylor series in terms of z :

$$G(z) = \sum_{k=0}^{k_{\max}} c_k z^k (q^2)^k \quad (35)$$

with

$$z(q^2) = \frac{\sqrt{t_{\text{cut}} + q^2} - \sqrt{t_{\text{cut}}}}{\sqrt{t_{\text{cut}} + q^2} + \sqrt{t_{\text{cut}}}}, \quad (36)$$

where k_{\max} truncates an infinite series expansion in z [70]. Here, $t_{\text{cut}} = 4m_\pi^2$, where m_π corresponds to the simulated pion mass, is chosen for the vector channel ($G = G_E$ or G_M), while $t_{\text{cut}} = 9m_\pi^2$, which is associated with the 3π continuum, will be chosen later for the axial-vector channel ($G = F_A$) [21].

We note here that k_{\max} must ensure that terms $c_k z^k$ become numerically negligible for $k > k_{\max}$ for a *model-independent fit*. Although $|c_k/c_{k-1}| < 1$ is expected for sufficiently large k , the range of possible values of k_{\max} is limited by the condition $k_{\max} \leq 8$ (7) for the G_E (G_M) form factor that are calculated at totally ten (nine) data points in this study. We then first check the stability of the fit results with a given k_{\max} .

Figure 8 shows the fit results for all ten data points of $G_E(q^2)$ with $k_{\max} = 2, 3$ and 8 in the z -expansion. Similarly, we also plot the fit results for all nine data points of $G_M(q^2)$ with $k_{\max} = 2, 3$ and 7 in Fig. 9. At a glance, one can see from Fig. 8 and Fig. 9 that the curvature becomes smaller in the z variable than the q^2 variable for both cases of G_E and G_M . This indicates

TABLE V. Results for the nucleon form factors in the vector channel. The values are all renormalized.

q^2 [(GeV) ²]	$G_E^{\text{ren}}(q^2)$	$G_M^{\text{ren}}(q^2)$	$F_1^{\text{ren}}(q^2)$	$F_2^{\text{ren}}(q^2)$
0.000	1.000(4)	N/A	1.000(4)	N/A
0.024(1)	0.924(11)	4.071(456)	0.944(12)	3.127(449)
0.048(2)	0.861(19)	3.640(350)	0.895(21)	2.744(341)
0.072(2)	0.804(27)	3.333(305)	0.851(28)	2.482(295)
0.095(3)	0.774(30)	3.313(344)	0.836(33)	2.478(327)
0.119(4)	0.733(32)	3.148(272)	0.806(33)	2.342(259)
0.143(5)	0.683(34)	3.059(275)	0.767(36)	2.292(263)
0.189(7)	0.652(46)	2.806(276)	0.751(44)	2.054(270)
0.209(8)	0.614(60)	2.980(398)	0.736(65)	2.245(370)
0.215(8)	0.601(50)	2.837(317)	0.716(50)	2.121(304)

TABLE VI. Results for the *isovector* electric RMS radius $\sqrt{\langle r_E^2 \rangle}$, magnetic moment μ_v and magnetic RMS radius $\sqrt{\langle r_M^2 \rangle}$ obtained from various uncorrelated fits.

Observable	dipole fit	quadratic fit	z-Exp fit			Experimental value	
			$k_{\max} = 2$	$k_{\max} = 3$	$k_{\max} = 8$	<i>ep</i> scatt.	μ - <i>H</i> atom
$\sqrt{\langle r_E^2 \rangle}$ [fm]	0.822(63)	0.851(62)	0.917(81)	0.914(101)	0.915(99)	0.939(6)	0.907(1)
χ^2/dof	2.60/8	0.99/7	0.42/7	0.41/6	0.41/1	—	—

Observable	dipole fit	quadratic fit	z-Exp fit			Experimental value
			$k_{\max} = 2$	$k_{\max} = 3$	$k_{\max} = 7$	
$\mu_v \equiv \mu_p - \mu_n$	3.96(46)	4.24(52)	4.53(61)	4.86(82)	4.81(79)	4.70589
$\sqrt{\langle r_M^2 \rangle}$ [fm]	0.656(133)	0.852(130)	1.177(195)	1.495(437)	1.437(409)	0.862(14)
χ^2/dof	1.04/7	0.52/6	0.41/6	0.36/5	0.37/1	—

TABLE VII. Results for the *isovector* Dirac RMS radius $\sqrt{\langle r_1^2 \rangle}$, anomalous magnetic moment $F_2^v(0)$ and Pauli RMS radius $\sqrt{\langle r_2^2 \rangle}$ obtained from various uncorrelated fits.

Observable	dipole fit	quadratic fit	z-Exp fit			Experimental value		
			$k_{\max} = 2$	$k_{\max} = 3$	$k_{\max} = 8$	<i>ep</i> scatt.	μ - <i>H</i> atom	LHPC'14 [11]
$\sqrt{\langle r_1^2 \rangle}$ [fm]	0.668(68)	0.740(75)	0.807(100)	0.782(129)	0.784(125)	0.798(7)	0.760(2)	0.706(40)
χ^2/dof	0.48/8	0.65/7	0.42/7	0.38/6	0.39/1	—	—	—

Observable	dipole fit	quadratic fit	z-Exp fit			Experimental value	LHPC'14 [11]
			$k_{\max} = 2$	$k_{\max} = 3$	$k_{\max} = 7$		
$\kappa_v \equiv F_2^v(0)$	3.01(45)	3.25(51)	3.52(60)	3.84(82)	3.79(79)	3.70589	3.89(39)
$\sqrt{\langle r_2^2 \rangle}$ [fm]	0.677(173)	0.896(157)	1.254(227)	1.606(499)	1.542(469)	0.879(17) ^a or 0.888(17) ^b	0.844(144)
χ^2/dof	1.01/7	0.54/6	0.44/6	0.40/5	0.40/1	—	—

^a Input of *ep* scatt.

^b Input of μ -*H* atom

that a power series in terms of z is clearly more efficient than one in q^2 . It is also observed that both fit results are not sensitive to the choice of k_{\max} . This suggests that the z expansion gives a rapid convergence series for both cases. Indeed, as shown in Fig. 10, the values of $|c_1/c_0|$ are insensitive to the choice of k_{\max} if $k_{\max} \geq 3$. For G_E , the ratios of $|c_k/c_{k-1}|$ with $k \geq 2$ become zero within the statistical error, while the ratios of $|c_k/c_{k-1}|$ for G_M reach a convergence value less than unity at $k \approx 5$ or 6. Thus, the value of $k_{\max} \leq 7$ is large enough to guarantee that the z-Exp analysis makes a *model-independent fit* and reduces systematic uncertainties to determine the RMS radii and the value of $G_M(0)$. For these reasons, $k_{\max} = 8$ (7) is hereafter chosen for the G_E (G_M) form factor in the z-Exp method.

In Fig. 11, we show the fit results for $G_E(q^2)$ (left panel) and $G_M(q^2)$ (right panel) with three types of fits: dipole (green dashed curve), quadratic (blue dot-dashed curve) and z-Exp (red solid curve) fits. All the fits reasonably describe all ten (nine) data points for G_E (G_M) with $\chi^2/\text{dof} < 1$. However, if one takes a closer look at low q^2 , the fit curve given by the z -expansion fit goes nicely through the data points in the low- q^2 region. This implies that the z-Exp fit is relatively insensitive on the higher q^2 data points as was expected. The RMS radius is determined to be $r_{\text{RMS}} = \sqrt{-6(c_1/c_0)/(4t_{\text{cut}})}$ (z-Exp fit), $\sqrt{-12a_1}$ (dipole fit) and $\sqrt{-6d_2/d_0}$ (quadratic fit), while the coefficients of c_0 , a_0 and d_0 for G_M correspond to the value of the magnetic moment, respectively. All results obtained from various uncorrelated fits, where we do not take into account correlations between the form factor data at different q^2 , are compiled in Table VI.

In Fig. 12, we compare the results for $\sqrt{\langle r_E^2 \rangle}$ (left panel) and μ_v (right panel) from the z-Exp fit (red

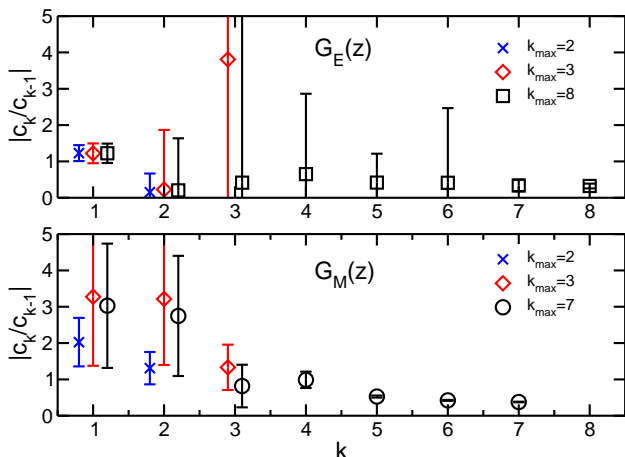


FIG. 10. Convergence behavior of the z-Exp fits for G_E (upper panel) and G_M (lower panel). The values of $|c_1/c_0|$ are insensitive to the choice of k_{\max} if $k_{\max} \geq 3$. For G_E , the ratios of $|c_k/c_{k-1}|$ with $k \geq 2$ become zero within the statistical error, while the ratios of $|c_k/c_{k-1}|$ for G_M reach a convergence value less than unity at $k \approx 5$ or 6.

square) with those from the quadratic (blue circle) and dipole (green diamond) fits. In the left panel, the two horizontal bands represent experimental results from ep scattering (upper) and muonic hydrogen (μ -H) atom (lower). The dipole results are underestimated in comparison to the corresponding experimental values. Although each z-Exp fit result has relatively larger error than the other results, its error may include both statistical and systematic uncertainties without any model dependence. Moreover each result of $\sqrt{\langle r_E^2 \rangle}$ and μ_v from the z-Exp fit is most consistent with its respective experiment. As our final results, we quote the value of the (isovector) electric RMS radius:

$$\sqrt{\langle r_E^2 \rangle} = 0.915 \pm 0.099 \text{ fm} \quad (37)$$

and the value of the (isovector) magnetic moment:

$$\mu_v = 4.81 \pm 0.79, \quad (38)$$

which are obtained from the z-Exp fits. The former is consistent with both the experimental values from ep scattering and μ -H atom spectroscopy, though statistical uncertainties should be reduced down to a few percent so as to resolve the experimental puzzle on the proton size.

3. Comparison with previous results

We finally compare our results for $\sqrt{\langle r_E^2 \rangle}$ and μ_v with recent lattice results from LHPC [11], PNDME [27], the Mainz group [28], ETMC (denoted as ETMC'13 [29] and ETMC'17 [12]) and the RBC-UKQCD (denoted as RBC-UKQCD'09 [15] and RBC-UKQCD'17 [30]) as shown in Fig. 13. See also Table VIII for a summary of previous lattice calculations in comparison with this study. Although our results are compatible with both experiments albeit with large errors, many results for both the electric RMS radius and magnetic momentum are often underestimated relative to their respective experimental values in the previous calculations as can be seen in Fig. 13.

The following are major points of concern for this issue: 1) both quantities are sensitive to the simulated pion mass, 2) their finite size effects become significant as the pion mass decreases, 3) the longer q^2 interpolations or extrapolations to estimate them cause larger systematic uncertainties. The last point is connected to the second point since the larger spatial volume enables us to access the nucleon form factors at smaller momentum transfers. In this context, the LHPC calculation, where the simulations were performed with the largest spatial size of 5.6 fm with almost physical quark masses, is a favorite among the previous calculations. Indeed, the LHPC results show better agreement with the experiments, though the electric RMS radius is slightly smaller than the PDG value.

The simulated pion mass in the LHPC calculation is comparable to that of ours. Our lattice setup is, however, superior to the LHPC calculation with respect to our spatial size of 8.1 fm. The larger spatial volume provides rich

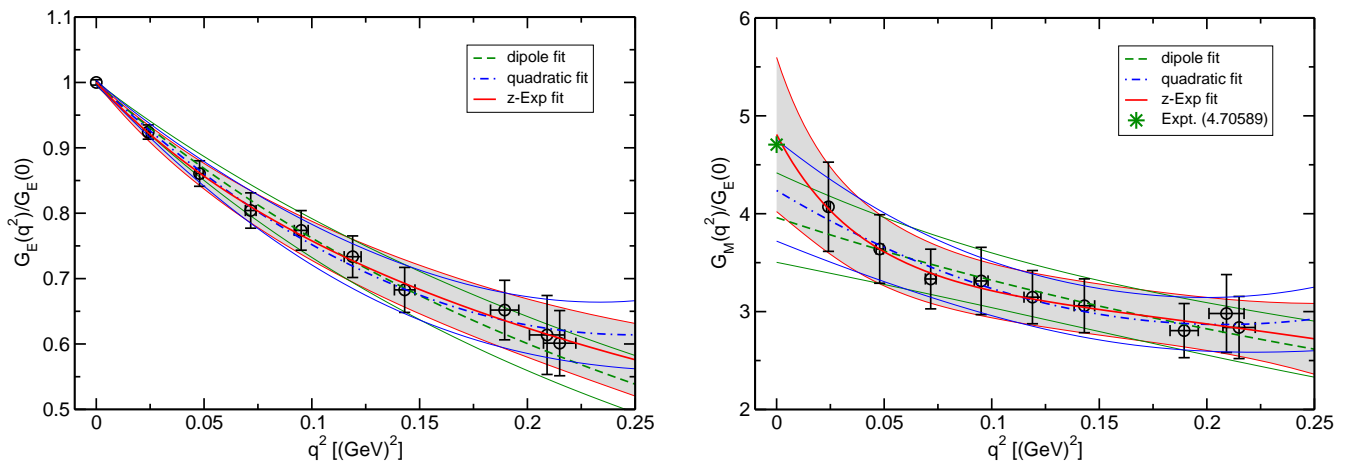


FIG. 11. Results for G_E (left panel) and G_M (right panel) with three types of fitting form ansatz: dipole (green), quadratic (blue) and z-Exp (red) fits. All fits are performed with all ten (nine) data points for G_E (G_M).

information about the momentum squared dependence of the nucleon form factors in the low q^2 region. Raw data for F_1 and F_2 are available in the tables of Ref. [11]. Therefore, it is worth comparing our results for the F_1 and F_2 form factors with their results in the same plots.

In Fig. 14, we show both the LHPC results (cross symbols) and our results (open circles) for the Dirac F_1 (left panel) and Pauli F_2 (right panel) form factors as a function of momentum squared q^2 . In each panel, the dashed curves correspond to Kelly's fit [55] as their experimental data. In the LHPC results, they use two types of kinematics regarding the momentum \mathbf{p}' for the final state of the nucleon state when constructing the three-point correlation functions (22). The smallest momentum transfer $q_{\min}^2 = 0.044$ [(GeV) 2] in the LHPC calculation is given by the choice of $\mathbf{p}' = 2\pi/L \times (-1, 0, 0)$, while we consider only the rest frame of the final state with $\mathbf{p}' = \mathbf{0}$.

Our results and the LHPC results are consistent with each other in both the F_1 and F_2 form factors within the statistical errors. We have found that the size of our statistical errors is similar to that of the LHPC data points which are calculated in the rest frame of the final state with $\mathbf{p}' = \mathbf{0}$. It is clear that the q^2 dependence of the form factors at low q^2 are much constrained by our results that contain the smallest nonzero q^2 data point. We primarily focus on the *isovector* Dirac RMS radius ($\sqrt{\langle r_1^2 \rangle}$) and anomalous magnetic moment ($\kappa_v = F_2^v(0)$) since the data for the F_2 form factor exhibits large statistical fluctuations in the low q^2 region.

We then extract the values of $\sqrt{\langle r_1^2 \rangle}$ and $\kappa_v = F_2^v(0)$ together with the Pauli RMS radius ($\sqrt{\langle r_2^2 \rangle}$) from the F_1 and F_2 form factors from various uncorrelated fits as summarized in Table VII. Our results for $\sqrt{\langle r_1^2 \rangle}$ and κ_v obtained from the z-Exp fits are more consistent with both experiments albeit with large errors. The dipole fits tend to yield smaller errors in comparison with the other fits. For comparison, the LHPC results for $\sqrt{\langle r_1^2 \rangle}$, $F_2^v(0)$ and $\sqrt{\langle r_2^2 \rangle}$ are also listed in Table. VII. Their quoted er-

rors on both $\sqrt{\langle r_1^2 \rangle}$ and κ_v are, however, smaller by a factor of 2 or 3 in comparison with our results obtained using the z-Exp fit. This is partly because the LHPC results are given by the dipole fits with large number of q^2 data points. Indeed, if we adopt the dipole fit rather than the z-Exp fit, the statistical uncertainties on the obtained results become small as those of the LHPC results. Although the LHPC results are also roughly consistent with experiments, the shorter q^2 interpolation (or extrapolation) that was achieved in our study by using the larger volume reduces the systematic uncertainties on the determination of $\sqrt{\langle r_1^2 \rangle}$ (or κ_v).

C. Results for nucleon form factors in the axial-vector and pseudoscalar channels

1. Axial-vector F_A and induced pseudoscalar F_P form factors

In the axial-vector channel, two independent form factors F_A and F_P can be extracted from kinematically different types of three-point functions (25). Recall that the z direction is chosen as the polarized direction through the definition of the projection operator \mathcal{P}_{5z} . Therefore, the longitudinal momentum (q_3) dependence explicitly appears in Eq. (25). The three-point functions are classified with the transverse ($i = 1$ or 2) and longitudinal ($i = 3$) components. Furthermore, for the case of $i = 3$, there are two types of kinematics: either $q_3 \neq 0$ or $q_3 = 0$.

We take advantage of the choice of either transverse or longitudinal directions together with explicit q_3 dependence so as to separately obtain F_A and F_P from Eq. (25) in line with Ref. [26]. For convenience, using the ratio of Eq. (25) we define

$$\Lambda_L^A(t, \mathbf{q}) = \sqrt{\frac{2E_N}{E_N + M_N}} \mathcal{R}_{A,3}^{5z}(t, \mathbf{q}) \quad (39)$$

TABLE VIII. Summary of previous lattice calculations for the nucleon electric-magnetic form factors in comparison with this study. Here, N_f denotes the number of dynamical quark flavors. In the fourth column, TM-Wilson (TM-Clover) stands for the twisted mass Wilson (clover) Dirac operator, DWF for the domain-wall fermions. In the last column, “R”, “S”, “TSF” and “GPoF” stand for the standard ratio method, the summation method, the two-state fit method and the generalized pencil-of-function method.

Publication	N_f	Type	Fermion	m_π [MeV]	a [fm]	La [fm]	Lm_π	t_{sep}/a	t_{sep} [fm]	Method
PNDME'13 [27]	2+1+1	Hybrid ^a	Clover	220	0.120	3.8	4.4	{8,9,10,11,12}	≤ 1.44	R, TSF
			Clover	310	0.120	2.9	4.6	{8,10,12}	≤ 1.44	R, TSF
LHPC'14 [11]	2+1	Full	Clover	≥ 149 ^b	0.116	5.6	4.21	{8,10,12}	≤ 1.39	R, S, GPoF
Mainz'15 [28]	2	Full	Clover	≥ 193 ^b	0.063	4.0	4.0	—	≤ 1.1	R, S, TSF
ETMC'13 [29]	2+1+1	Full	TM-Wilson	213	0.064	3.1	3.35	18	1.15	R
			TM-Wilson	373	0.082	2.6	4.97	12	0.98	R
ETMC'17 [12]	2	Full	TM-Clover	130	0.094	4.5	2.97	{10,12,14,16,18} ^c	≤ 1.69 ^c	R, S, TSF
RBC-UKQCD'09 [15]	2+1	Full	DWF	≥ 330 ^b	0.114	2.7	4.58	12	1.37	R
RBC-UKQCD'17 [30]	2+1	Full	DWF	172	0.143	4.6	4.00	{7,9}	≤ 1.29	R
			DWF	249	0.143	4.6	5.79	{7,9}	≤ 1.29	R
This work	2+1	Full	Clover	146	0.085	8.1	6.0	15	1.27	R

^a Clover fermions on highly improved staggered quark (HISQ) ensembles

^b In Fig. 13, we only quote the results at the lightest pion mass.

^c The electric form factor determined with the projection operator \mathcal{P}_t is evaluated up to $t_{\text{sep}}/a = 18$ ($t_{\text{sep}} = 1.69$ [fm]), while the magnetic, axial-vector and pseudoscalar form factors determined with the projection operator \mathcal{P}_{5z} are evaluated only up to $t_{\text{sep}}/a = 14$ ($t_{\text{sep}} = 1.32$ [fm]).

and

following relation to the form factors:

$$\Lambda_L^A(\mathbf{q}) = F_A(q^2) - \frac{q_3^2}{M_N + E_N} F_P(q^2), \quad (41)$$

$$\Lambda_T^A(t, \mathbf{q}) = -\frac{\sqrt{2M_N^2 E_N (E_N + M_N)}}{2} \times \left(\frac{\mathcal{R}_{A,1}^{5z}(t, \mathbf{q})}{q_2 q_3} + \frac{\mathcal{R}_{A,2}^{5z}(t, \mathbf{q})}{q_1 q_3} \right). \quad (40)$$

$$\Lambda_T^A(\mathbf{q}) = M_N F_P(q^2). \quad (42)$$

In the plateau region of $\Lambda_{L,T}^A(t, \mathbf{q})$ we determine the matrix elements of the axial-vector current which has the

The simplest method is to obtain F_A is obtained from $\Lambda_L^A(\mathbf{q})$ with $q_3 = 0$, while F_P is evaluated from $\Lambda_T^A(\mathbf{q})/M_N$. However, due to the kinematics, $q_3 = 0$ is not available for Q3, Q6 and Q9 (labels defined in Table II), while $\Lambda_T^A(\mathbf{q})$ is not calculable for Q1, Q4, Q8. We then determine the two form factors through the following equations which explicitly depend on the longitudinal momentum q_3 :

$$F_A(q^2) = \begin{cases} \Lambda_L^A(q_3 \neq 0) + \frac{q_3^2}{M_N(M_N + E_N)} \Lambda_T^A(\mathbf{q}) & \text{for Q3, Q6, Q9} \\ \Lambda_L^A(q_3 = 0) & \text{for Q1, Q4, Q8} \end{cases} \quad (43)$$

$$F_P(q^2) = \begin{cases} \Lambda_T^A(\mathbf{q})/M_N & \text{for Q3, Q6, Q9} \\ \frac{M_N + E_N}{q_3^2} (\Lambda_L^A(q_3 = 0) - \Lambda_L^A(q_3 \neq 0)) & \text{for Q1, Q4, Q8.} \end{cases} \quad (44)$$

Although both ways are available for Q2, Q5 and Q7, we choose the former in this study.

Figure 15 shows the ratios of the three- and two-point functions (43) and (44) as a function of the current insertion time slice t for the axial-vector form factor

(F_A) (left) and induced-pseudoscalar form factor (F_P) (right) at the nine lowest nonzero momentum transfers. The latter is multiplied by $2M_N$ to make it a dimensionless quantity, while both ratios are renormalized with $Z_A = 0.9650(68)(95)$, which is given in the SF

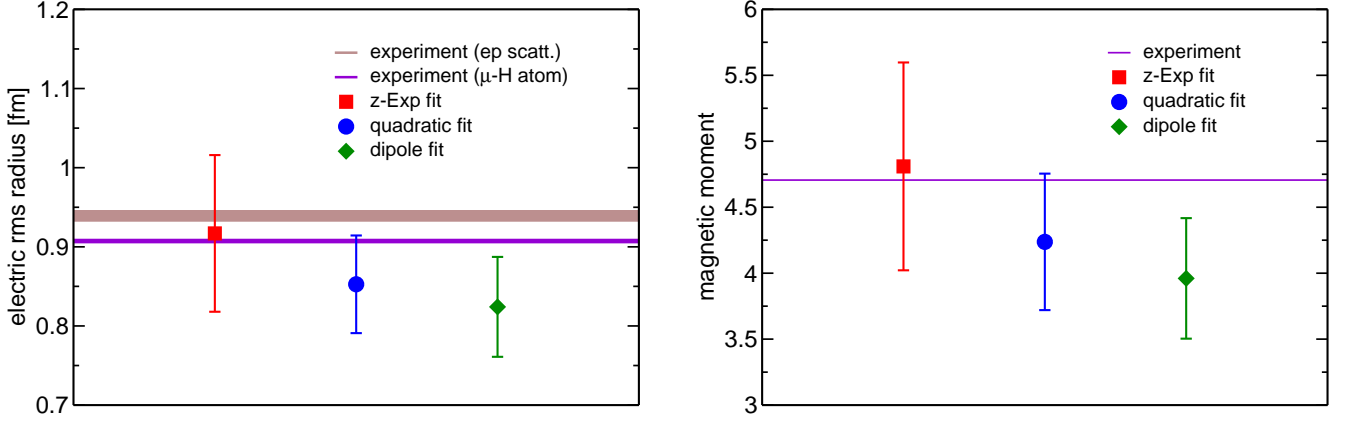


FIG. 12. Comparison of results obtained with three types of fitting form ansatz for the electric RMS radius $\sqrt{\langle r_E^2 \rangle}$ (left panel) and magnetic moment μ_v (right panel). In the left panel, two horizontal bands represent experimental results from ep scattering (upper) and μ - H atom spectroscopy (lower).

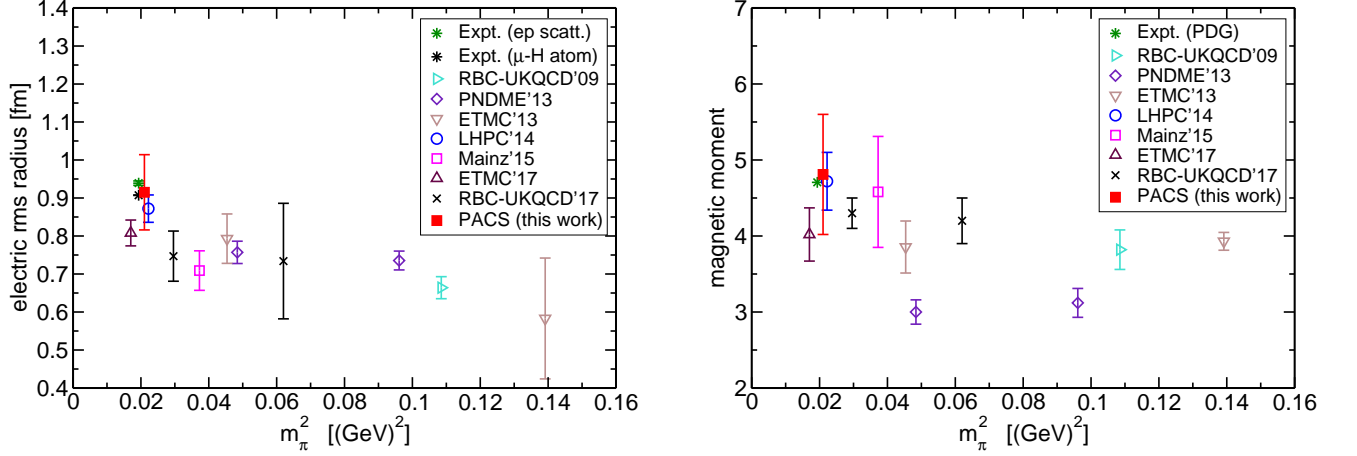


FIG. 13. Our results for $\sqrt{\langle r_E^2 \rangle}$ (left) and μ_v (right) at $m_\pi \approx 146$ MeV (filled square) compared to recent lattice results [11, 12, 27–30]. The asterisks represent the experimental results [4].

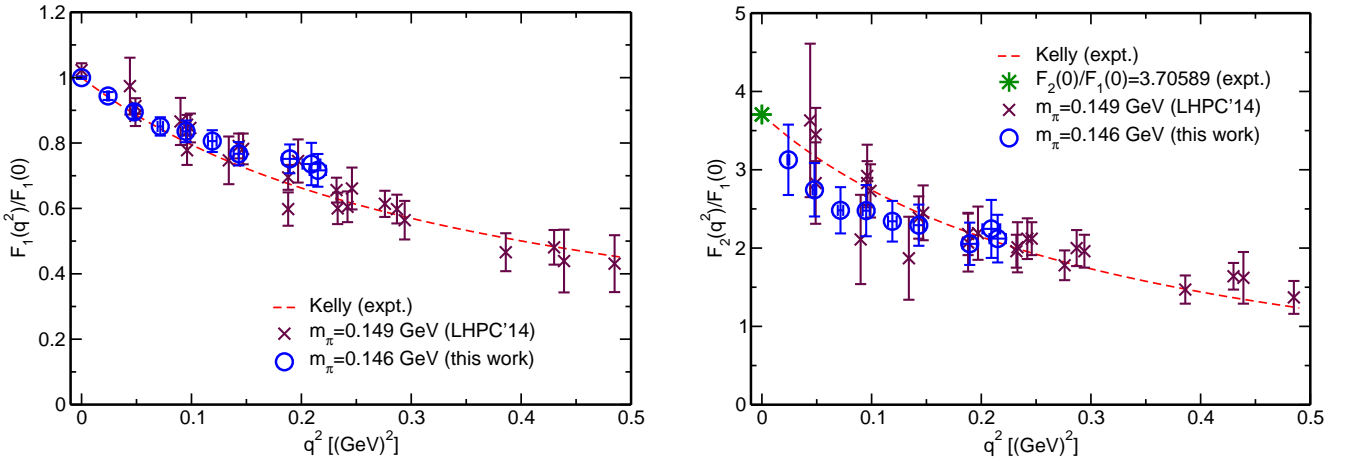


FIG. 14. Comparison of the *isovector* Dirac form factor F_1 (left) and Pauli form factor F_2 (right) results between from this work (circles) and LHC'14 (crosses) taken from Ref. [11]. The dashed curve in each panel shows Kelly's parametrization of the experimental data, while the asterisk in the right panel represents the experimental result.

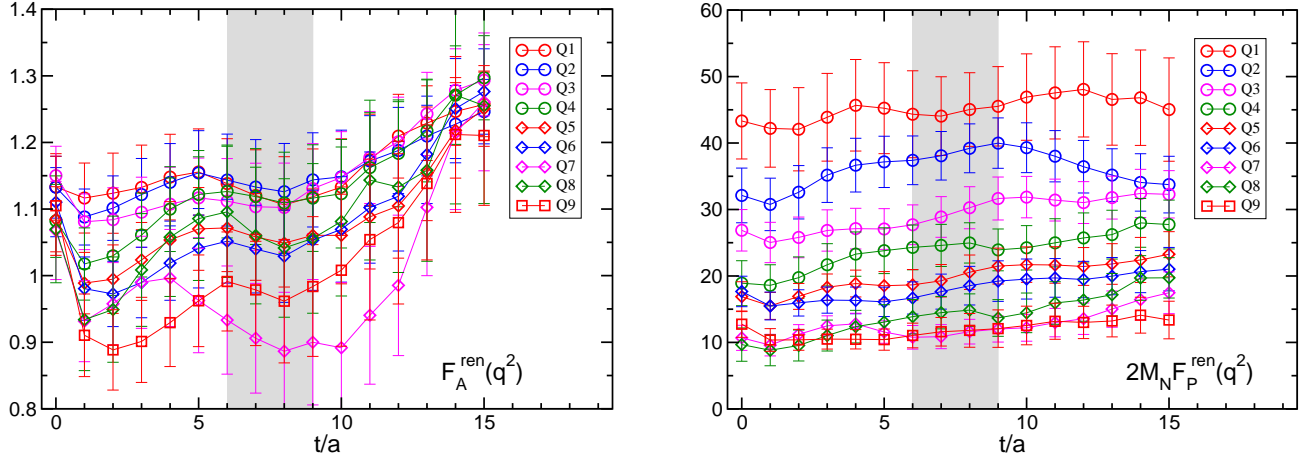


FIG. 15. Ratios of the three- and two-point functions (43) and (44) for the axial-vector form factor F_A (left) and induced pseudoscalar form factor F_P (multiplied by $2M_N$ to make it a dimensionless quantity) (right) at the nine lowest nonzero momentum transfers. Both ratios are renormalized with $Z_A = 0.9650(68)(95)$ [53]. The gray shaded area ($6 \leq t/a \leq 9$) in each panel shows the region where the values of the corresponding form factor are estimated.

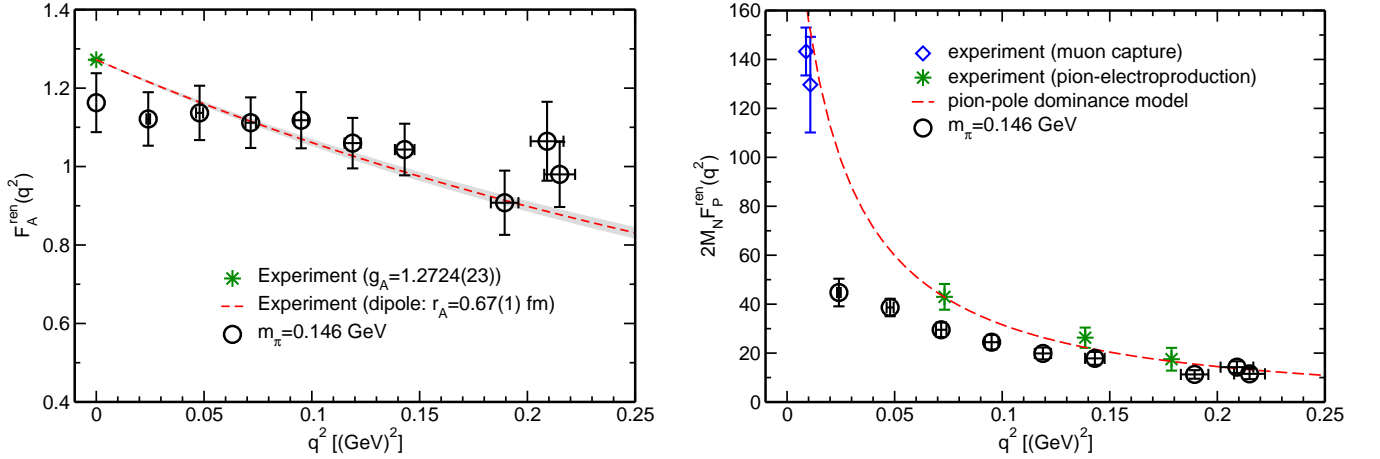


FIG. 16. Momentum-squared dependence of the axial vector form factor F_A (left) and induced pseudoscalar form factor F_P (right). Both form factors are renormalized with $Z_A = 0.9650(68)(95)$ [53]. In the left panel, the experimental curve is given by a dipole form with the RMS radius of $0.67(1)$ fm [19, 20], while the red dashed curve in the right panel is given by the pion-pole dominance model. The experimental data points in the right panel are given by muon capture [58, 59] and pion electroproduction [24].

scheme [53]. We evaluate the values of both axial-vector and induced-pseudoscalar form factors by constant fits to the data points in the time region $6 \leq t/a \leq 9$ denoted by the gray shaded area.

We next show the q^2 dependence of the renormalized form factors, F_A^{ren} (left panel) and F_P^{ren} (right panel), in Fig. 16. The values of $F_A^{\text{ren}}(q^2)$ and $2M_N F_P^{\text{ren}}(q^2)$ are also summarized in Table IX. In the left panel, the experimental curve is given by a dipole form with a RMS radius of $0.67(1)$ fm [19, 20] for a comparison. At a glance, the F_A^{ren} form factor is barely consistent with the experimental curve in the whole region of measured momentum transfers within the current statistics, except for two points at the smallest and second smallest momentum transfers including the axial-vector coupling $g_A = F_A(0)$.

In the right panel, two experiments results from muon capture and pion-electroproduction are marked as blue diamonds and green asterisks. Our result for $F_P(q^2)$ is significantly underestimated in comparison with both experiments especially in the low- q^2 region. The F_P form factor is expected to have a pion pole that dominates the behavior near zero momentum transfer. The red dashed curve in the right panel is given by the pion-pole dominance (PPD) model, where the induced pseudoscalar form factor is given as

$$F_P^{\text{PPD}}(q^2) = 2M_N F_A(q^2)/(q^2 + m_\pi^2), \quad (45)$$

whose functional form becomes justified by the generalized GT relation (17) at least in the chiral limit ($\hat{m} = 0$). Indeed, the two experimental results from muon capture

TABLE IX. Results for the nucleon form factors in the axial-vector channel and pseudoscalar channel. The form factors F_A^{ren} and F_P^{ren} are renormalized ones, while G_P is not yet renormalized.

q^2 [(GeV) ²]	$F_A^{\text{ren}}(q^2)$	$2M_N F_P^{\text{ren}}(q^2)$	$G_P(q^2)$
0.000	1.163(75)	N/A	N/A
0.024(1)	1.121(68)	44.8(5.6)	80.0(5.8)
0.048(2)	1.137(69)	38.6(3.6)	57.7(4.0)
0.072(2)	1.112(64)	29.5(3.0)	46.4(3.3)
0.095(3)	1.118(72)	24.5(3.0)	39.9(4.1)
0.119(4)	1.060(64)	19.9(2.4)	35.6(2.9)
0.143(5)	1.043(66)	17.9(2.6)	32.8(3.0)
0.189(7)	0.908(82)	11.3(1.7)	26.4(3.0)
0.209(8)	1.065(101)	14.3(2.4)	18.6(4.0)
0.215(8)	0.980(83)	11.5(2.1)	26.8(3.7)

and pion-photo production follow a curve given by the PPD model. According to the PPD model (45), the observed quenching effect in the value of $F_P(q^2)$ might be *partly* due to the underestimation of the axial-vector coupling g_A obtained in this study.

We next evaluate the axial RMS radius $\sqrt{\langle r_A^2 \rangle}$ from the slope of $F_A(q^2)/F_A(0)$ at zero momentum transfer. Three types of fits are used as in the cases of $\sqrt{\langle r_E^2 \rangle}$ and $\sqrt{\langle r_M^2 \rangle}$. First of all, Fig. 17 shows the z-Exp fit results for all ten data points of $F_A(q^2)/F_A(0)$ with $k_{\text{max}} = 2, 3$ and 8 in the z-expansion. In Fig. 17, the ratio of $F_A(q^2)/F_A(0)$ is plotted as a function of the variable z , which is defined by Eq. (36) with $t_{\text{cut}} = 9m_\pi^2$.

Before discussing the stability of the z-Exp fit, we remark that the statistical uncertainties on $F_A(q^2)/F_A(0)$ at the lower momentum transfers are extremely suppressed since statistical fluctuations in the numerator and denominator are highly correlated. This observation indicates that the underestimation of $F_A(q^2)$ at the second smallest momentum transfer compared with the experimental value found in Fig. 16 can be attributed to the reduction of the axial-vector coupling g_A .

As shown in the three panels of Fig. 17, we again confirm that the fit results are not sensitive to the choice of k_{max} as in the cases of G_E and G_M . Therefore, the value of $k_{\text{max}} = 8$ is large enough to guarantee that the z-Exp analysis makes a model-independent fit.

For comparison, in Fig. 18, we next show the fit results for $F_A(q^2)/F_A(0)$ with three types of fits: dipole (green dashed curve), quadratic (blue dot-dashed curve) and z-Exp (red solid curve) fits. All results of the axial RMS radius obtained using the three fits are compiled in Table X. Although all three fits are mutually consistent with each other because of their large statistical errors, the z-Exp fit tends to give a higher value, $\sqrt{\langle r_A^2 \rangle} = 0.46(11)$ fm, which is closer to the experimental value of 0.67(1) fm [71].

2. Pseudoscalar G_P form factor

As described in Sec. II, it is theoretically known that the two form factors F_A and F_P in the axial-vector channel are not fully independent. Theoretically, the q^2 dependences of F_A and F_P should be constrained by the generalized GT relation (17) with the pseudoscalar form factor G_P as a consequence of the axial Ward-Takahashi identity. To test whether the correct behavior of the generalized GT relation is well satisfied in our simulations, we also calculate the pseudoscalar matrix element, which is described by the single form factor $G_P(q^2)$ defined in Eq. (18).

Figure 19 shows the ratio of the three- and two-point functions (26) as a function of the current insertion time slice t for the pseudoscalar form factor $G_P(q^2)$ at the nine lowest nonzero momentum transfers after extracting the relevant kinematical factors. The plateau region is clearly defined even at the higher momentum transfers with our choice of source-sink separation. We thus evaluate the values of the pseudoscalar form factors by constant fits to the data points in the time region $6 \leq t/a \leq 9$ denoted by the gray shaded area as in the cases of the other form factors. We next plot the bare pseudo-scalar form factor $G_P(q^2)$, which is not renormalized, in Fig. 20. The measured q^2 dependence of $G_P(q^2)$ resembles that of $F_P(q^2)$, where the relatively strong q^2 dependence appears in the lower q^2 region as was expected from the pion-pole contribution.

In the PPD model, the pion-pole dominance holds even in $G_P(q^2)$. Combined with Eq. (17) and Eq. (45), a naive pion-pole dominance form $G_P^{\text{PPD}}(q^2)$ is given as

$$2\hat{m}G_P^{\text{PPD}}(q^2) = 2M_N F_A(q^2) \frac{m_\pi^2}{q^2 + m_\pi^2}. \quad (46)$$

Thus one may realize that the ratio of the PPD forms, G_P^{PPD} and F_P^{PPD} does not depend on q^2 and gives the low-energy constant B_0 as

$$\frac{G_P^{\text{PPD}}(q^2)}{F_P^{\text{PPD}}(q^2)} = B_0 \quad (47)$$

with the help of the Gell-Mann–Oakes–Renner (GMOR) relation for the pion mass: $m_\pi^2 = 2B_0\hat{m}$.

As shown in Fig. 21, the ratio of $G_P(q^2)/F_P^{\text{ren}}(q^2)$ indeed exhibits a flat q^2 dependence at lower q^2 . We then estimate the low-energy constant B_0 by a constant fit to the plateau value using six data points at the lower momentum transfer. We then get the bare value of the low-energy constant as $B_0 = 3.10(25)$ [GeV], which is represented by blue solid line with a shaded band in Fig. 21 and tabulated in Table XI. This value is fairly consistent with the one evaluated by the GMOR relation with the simulated pion mass and a (bare) quark mass ($am_{\text{PCAC}} = 0.001577(10)$) obtained from the pion two-point correlation functions with the PCAC relation [13, 53]. This observation strongly indicates that

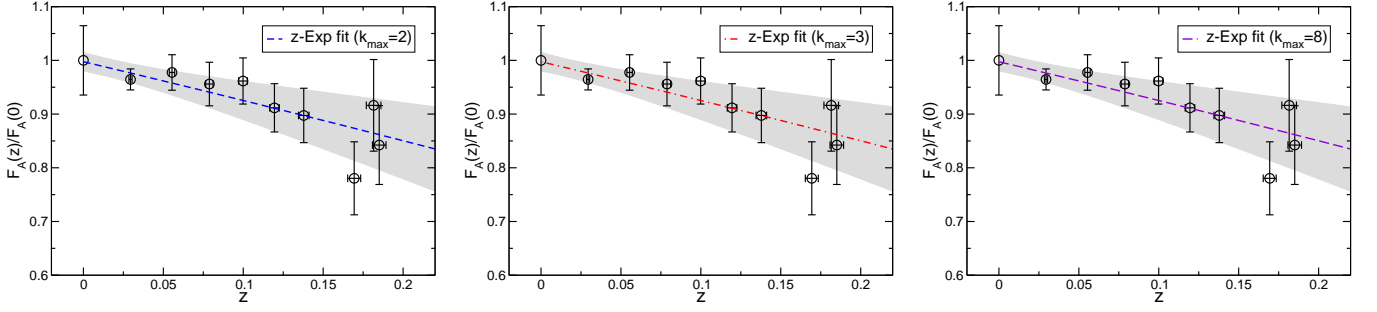


FIG. 17. Results for z-Exp fit of F_A with $k_{\max} = 2$ (left), 3 (middle) and 8 (right) using all ten data points.

TABLE X. Results of axial radius $\sqrt{\langle r_A^2 \rangle}$ obtained from various uncorrelated fits.

Observable	dipole fit	quadratic fit	z-Exp fit			Experimental value
			$k_{\max} = 2$	$k_{\max} = 3$	$k_{\max} = 8$	
$\sqrt{\langle r_A^2 \rangle}$ [fm]	0.40(12)	0.22(49)	0.46(11)	0.46(11)	0.46(11)	0.67(1)
χ^2/dof	3.45/8	2.60/7	4.00/7	4.00/6	4.00/1	—

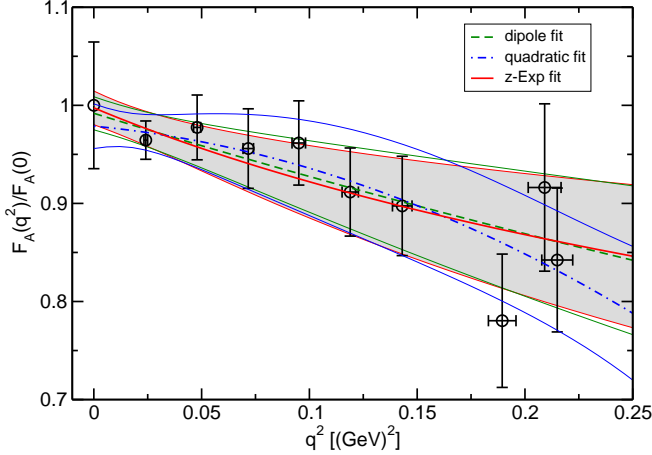


FIG. 18. Results for F_A with three types of fitting form ansatz: dipole (red), quadratic (blue) and z-Exp (green) fits. All fits are performed with all ten data points.

the $G_P(q^2)$ form factor shares a similar pion-pole structure with the $F_P^{\text{ren}}(q^2)$ form factor and the ratio of their residues is highly constrained by the GMOR relation.

3. Test for the axial Ward-Takahashi identity

In order to verify the axial Ward-Takahashi identity in terms of the nucleon matrix elements, we define the following ratio inspired by the generalized GT relation (17)

$$m_{\text{AWTI}} = \frac{2M_N F_A^{\text{ren}}(q^2) - q^2 F_P^{\text{ren}}(q^2)}{2G_P(q^2)} \quad (48)$$

with the simulated nucleon mass M_N . If the ratio reveals a q^2 -independent plateau in the entire q^2 region, m_{AWTI}

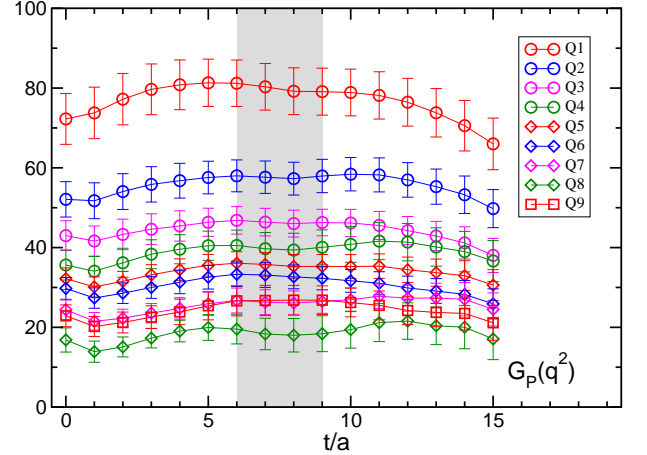


FIG. 19. Ratio of the three- and two-point functions (26) for the pseudoscalar form factor G_P at the nine lowest nonzero momentum transfers after extracting the relevant kinematical factors. The gray shaded area ($6 \leq t/a \leq 9$) in each panel shows the region where the values of the corresponding form factor are estimated.

should be regarded as an alternative (bare) quark mass.

As shown in Fig. 22, the ratio m_{AWTI} has no appreciable q^2 dependence. It indicates that three form factors well satisfy the generalized GT relation. Using data points at the six lowest momentum transfers, we can read off $am_{\text{AWTI}} = 0.00451(48)$, which is roughly 3 times heavier than the PCAC quark mass [13, 53]. Since the PCAC relation is also a consequence of the axial Ward-Takahashi identity, the relation $m_{\text{PCAC}} \approx m_{\text{AWTI}}$ was expected. However, this is not the case.

Although the above consideration does not take into account $\mathcal{O}(a)$ improvement of the axial-vector current, we next verify that this issue has nothing to do with

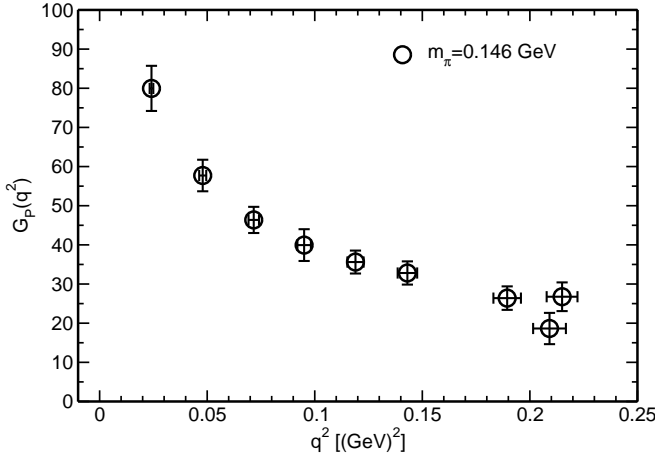


FIG. 20. Momentum-squared dependence of the pseudoscalar form factor, which is the bare value, *i.e.* not renormalized.

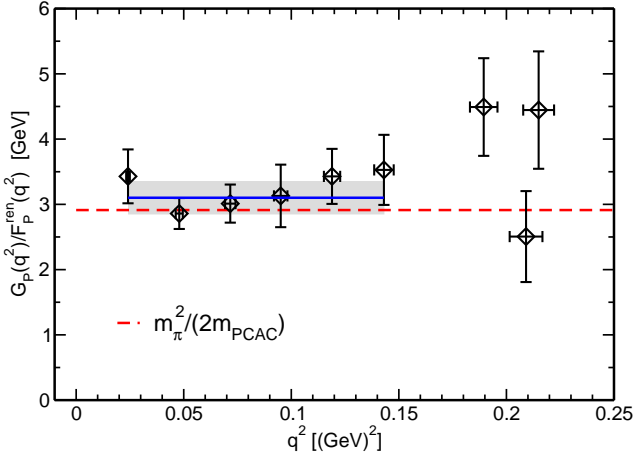


FIG. 21. The ratio of $G_P(q^2)/F_P^{\text{ren}}(q^2)$ as a function of momentum squared q^2 . A flat q^2 dependence is observed due to the fact that the $G_P(q^2)$ form factor shares a similar pion-pole structure with the $F_P^{\text{ren}}(q^2)$ form factor. The blue solid line represents the (constant) fit result and the shaded band denotes the fit range and statistical error estimated using the jackknife method, while a red dashed line represents the bare low-energy constant evaluated using the ratio of $m_\pi^2/(2m_{\text{PCAC}})$.

finite lattice spacing artifacts. The renormalized $\mathcal{O}(a)$ -improved operator takes the form

$$\mathcal{A}_\alpha^+(x) = Z_A [A_\alpha^+(x) + ac_A \partial_\alpha P^+(x)], \quad (49)$$

where $A_\alpha^+(x) = \bar{u}(x)\gamma_\alpha\gamma_5 d(x)$ and $P^+(x) = \bar{u}(x)\gamma_5 d(x)$. Strictly speaking, this improved axial-vector current satisfies the axial Ward-Takahashi identity on the lattice: $\partial_\alpha \mathcal{A}_\alpha^+(x) = 2\hat{m}P^+(x)$. Therefore, the generalized GT relation (17) is slightly modified by the presence of the $\mathcal{O}(a)$ improvement term in Eq. (49). However, the term proportional to c_A only contributes to the modification of the F_P form factor as $F_P^{\text{imp}}(q^2) = F_P(q^2) + ac_A G_P(q^2)$,

and then the modified GT relation is expressed by

$$Z_A \left(2M_N F_A(q^2) - q^2 F_P^{\text{imp}}(q^2) \right) = 2\hat{m}G_P(q^2). \quad (50)$$

Starting from the modified GT relation (50), the (bare) quark mass \hat{m} becomes

$$\begin{aligned} m_{\text{AWTI}}^{\text{imp}} &= \frac{Z_A \left(2M_N F_A(q^2) - q^2 F_P^{\text{imp}}(q^2) \right)}{2G_P(q^2)} \\ &= \frac{2M_N F_A^{\text{ren}}(q^2) - q^2 F_P^{\text{ren}}(q^2)}{2G_P(q^2)} - \frac{aZ_A c_A}{2} q^2, \end{aligned} \quad (51)$$

where the first term is nothing but the ratio m_{AWTI} defined in Eq. (48) and the second term corresponds to a correction term due to $\mathcal{O}(a)$ improvement of the axial-vector current. Although the ratio m_{AWTI} may indeed receive the $\mathcal{O}(a)$ correction, which yields a linear dependence on q^2 , the effect of $\mathcal{O}(a)$ improvement is insignificant in the low q^2 region. Furthermore, the improvement coefficient c_A is found to be very small with our choice of $c_{\text{SW}} = 1.11$ [36]. The improvement coefficient c_A is expected to be of the order of a few 0.01 in lattice units [36].

In Fig. 23, we plot the ratio $m_{\text{AWTI}}^{\text{imp}}$ defined in Eq. (51) as a function of momentum squared q^2 . Circles represent the unimproved results obtained in Eq. (51) with $c_A = 0.0$ in lattice units. After adopting the renormalized $\mathcal{O}(a)$ -improved operator (49), the central value of the unimproved results at each q^2 point is likely to move in the brown band, which represents the region between the lower ($c_A = 0.03$ in lattice units) and upper ($c_A = -0.03$ in lattice units) limits. Figure 23 indicates that the systematic uncertainties that arise from the $\mathcal{O}(a)$ -improvement term in the axial-vector current are much smaller than the current statistical errors in this study. The large deviation from the blue dashed line, which denotes the PCAC quark mass, mostly stays the same. We thus conclude that the issue of $m_{\text{AWTI}} \gg m_{\text{PCAC}}$ is not directly related to finite lattice spacing artifacts. We rather speculate that this issue is connected with the modification of the pion-pole structure in both the $F_P(q^2)$ and $G_P(q^2)$ form factors as will be described in the next subsection. Hereafter, the improvement coefficient is set to $c_A = 0$ in our entire analysis.

4. Distortion of pion-pole structure

In the previous subsections, we have observed that the q^2 dependences of F_A , F_P and G_P are well constrained by the generalized GT relation, while the ‘‘pion-pole’’ structures of F_P and G_P are likely the same. However, the bare quark mass (m_{AWTI}) evaluated from the ratio (48) is roughly 3 times heavier than the value of m_{PCAC} . This puzzle could be related to the discrepancy between our result for $F_P(q^2)$ and experiments.

We first speculate that the measured $F_P(q^2)$ can be

TABLE XI. Results for the bare low-energy constant (B_0), the uncorrected quark mass (m_{AWTI}), the pole mass of F_P (m_{pole}), the modification factor α_{pole} and the corrected quark mass (m_{quark}).

B_0 [GeV]	am_{AWTI}	am_{pole}	m_{pole} [MeV]	α_{pole}	am_{quark}
3.10(25)	0.00451(48)	0.1099(74)	256(17)	3.05(41)	0.00145(12)

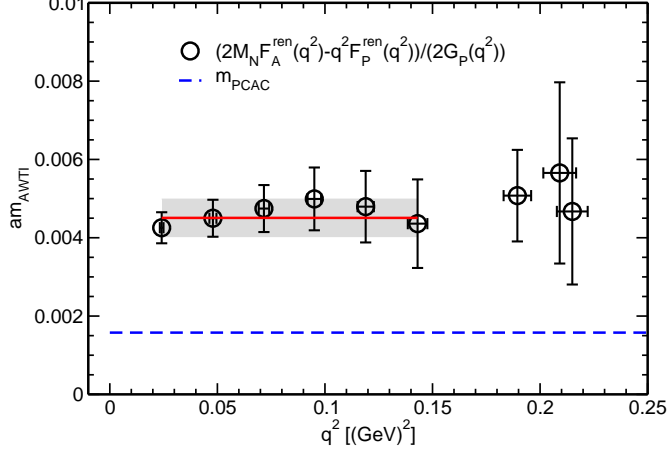


FIG. 22. The ratio m_{AWTI} defined in Eq. (48) as a function of momentum squared q^2 . The blue dashed line denotes the PCAC quark mass [13, 53] in lattice units.

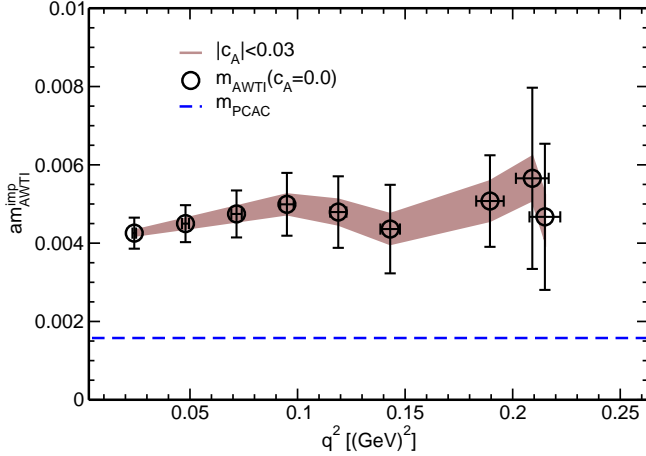


FIG. 23. The ratio $m_{\text{AWTI}}^{\text{imp}}$ defined in Eq. (51) as a function of momentum squared q^2 . The improvement coefficient c_A is expected to be of the order of a few 0.01 in lattice units. The central value of the unimproved results (denoted by circles) at each q^2 point is likely to move in the brown band, which represents the region between the lower ($c_A = 0.03$ in lattice units) and upper ($c_A = -0.03$ in lattice units) limits.

described by the PPD inspired form:

$$F_P(q^2) \approx \frac{2M_N F_A(q^2)}{q^2 + m_{\text{pole}}^2} \quad (52)$$

with the pole mass m_{pole} , which is not necessarily constrained by our simulated pion mass m_π . If this func-

tional form well describes the measured $F_P(q^2)$, we may define the effective ‘‘pion-pole’’ mass from $F_P(q^2)$ as

$$m_{\text{pole}} = \sqrt{\frac{2M_N F_A(q^2)}{F_P(q^2)} - q^2}, \quad (53)$$

which would exhibit a flat q^2 dependence.

In Fig. 24, we plot the effective pole mass as a function of q^2 . The horizontal dash-dotted line represents the value of the simulated pion mass m_π in lattice units. Clearly, there is no appreciable q^2 dependence of the effective pole mass m_{pole} . In particular, the six data points at lower q^2 are fairly consistent within statistical errors. We then get the pole mass value as $am_{\text{pole}} = 0.1099(74)$, which is given by a constant fit to data in the shaded region. However, the value $m_{\text{pole}} = 256(17)$ MeV is roughly twice as heavy as the simulated pion mass ($m_\pi \approx 146$ MeV). This indicates that the ‘‘pion-pole’’ structure in $F_P(q^2)$ is modified by the larger pole mass. We then define the modification factor α_{pole} as follows

$$\alpha_{\text{pole}} \equiv \frac{m_{\text{pole}}^2}{m_\pi^2} \quad (54)$$

and obtain its value as $\alpha_{\text{pole}} = 3.05(41)$ which can account for the discrepancy between m_{AWTI} and m_{PCAC} through the GMOR relation. We thus estimate an improved value of the bare quark mass as

$$m_{\text{quark}} = m_{\text{AWTI}}/\alpha_{\text{pole}}, \quad (55)$$

which should be very consistent with the value of m_{PCAC} .

Next, we plot the quantity of m_{quark} in lattice units as a function of q^2 in Fig. 25. Again, there is no appreciable q^2 dependence especially at low q^2 . The horizontal dashed line represents the value of m_{PCAC} , while the solid line indicates the fit result of m_{quark} and shaded band displays the fit range and 1 standard deviation. The value of m_{quark} is obtained as

$$am_{\text{quark}} = 0.00145(12), \quad (56)$$

which is in good agreement with the value $am_{\text{PCAC}} = 0.001577(10)$.

The importance of our findings is twofold: 1) our results for all three form factors, $F_A(q^2)$, $F_P(q^2)$ and $G_P(q^2)$, are subjected to the generalized GT relation (17) as a consequence of the axial Ward-Takahashi identity, and 2) the discrepancy between our result for $F_P(q^2)$ and experiments is mainly caused by the distortion of the pion-pole structure in both $F_P(q^2)$ and $G_P(q^2)$, though

the reason is not yet known. Therefore, in this work, we prefer not to estimate the pseudoscalar coupling g_P and pion-nucleon coupling $g_{\pi NN}$, since both quantities are highly sensitive to the pole structure of $F_P(q^2)$.

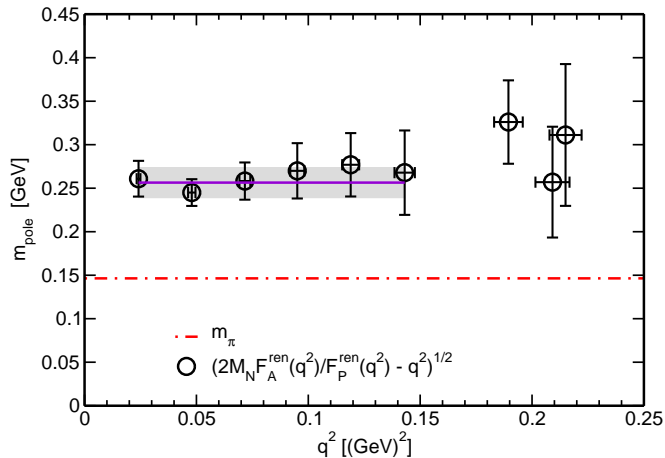


FIG. 24. Effective pole-mass plot as a function of momentum squared q^2 . The horizontal dash-dotted line represents the value of the simulated pion mass in physical units [GeV].

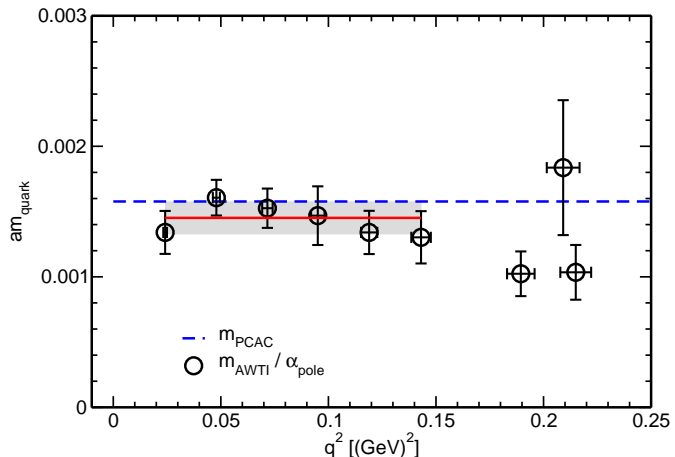


FIG. 25. The modified quark mass $m_{\text{quark}} = m_{\text{AWTI}}/\alpha_{\text{pole}}$ as a function of momentum squared q^2 . The blue dashed line denotes the PCAC quark mass [13, 53] in lattice units.

V. SUMMARY AND CONCLUDING REMARKS

We have studied the nucleon form factors calculated in 2+1 flavor QCD near the physical point ($m_\pi \approx 146$ MeV) in a large spatial volume $(8.1 \text{ fm})^3$ at a single lattice spacing of 0.085 fm. We computed the relevant three-point correlation functions using the sequential source method with a fixed source-sink separation of 1.27 fm.

We first analyzed the vector nucleon matrix element, which is described by the electric (G_E) and magnetic (G_M) form factors. We carefully examined the shapes

of both the G_E and G_M form factor with a model-independent analysis based on the z -expansion method. As a result, we obtained the isovector electric RMS radius $\sqrt{\langle r_E^2 \rangle}$ and magnetic moment μ_v , which are consistent with experimental values. We would like to emphasize that the former quantity is, for the first time, consistent with both the experimental values from ep scattering and μ - H atom spectroscopy, though further reduction of statistical and systematic errors (including electromagnetic and isospin-breaking effects) down to less than 1% is required to resolve the experimental puzzle on the proton size.

We have also analyzed the axial-vector nucleon matrix element, which is described by the axial-vector (F_A) and induced pseudoscalar (F_P) form factors. We have found that although the axial charge $g_A = F_A(0)$ is slightly underestimated in comparison with the experimental value, the axial vector form factor F_A is barely consistent with experiments in the low- q^2 region ($0 \leq q^2 \leq 0.2 \text{ [(GeV)}^2\text{]}$). However, the pseudoscalar form factor F_P is considerably underestimated at very low q^2 .

To understand this issue, we have, in addition, calculated the pseudoscalar matrix element, which is described by a single form factor of G_P called the pseudoscalar form factor. We examined q^2 dependences of three form factors, F_A , F_P and G_P , which should be constrained by the generalized GT relation as a consequence of the axial Ward-Takahashi identity. We have observed that the G_P form factor shares a similar “pion-pole” structure with the F_P form factor. The “pion-pole” structure was, however, found to be distorted due to the pole mass being larger than the simulated pion mass. If this effect is taken into account for an estimation of the bare quark mass by using three form factors through the generalized GT relation, we can fully verify the axial Ward-Takahashi identity in terms of the nucleon matrix elements. The bare quark mass obtained in this study as shown in Table XI is consistent with an alternative quark mass obtained from the pion two-point correlation functions with the PCAC relation. We, however, have not yet fully understood the origin of the “pion-pole” distortion found in the F_P and G_P form factors. The similar issue in the axial-vector channel was reported in Refs. [9, 61]. After we completed this work, Bär has advocated that the distortion of the pion-pole structure that was observed in this work can be qualitatively explained by the $N\pi$ excited state contamination [62].

The PACS Collaboration is generating new ensembles in a significantly large spatial volume of $(10.8 \text{ fm})^3$ at the physical point ($m_\pi \approx 135$ MeV) [63, 64]. Thus, we plan to develop the present calculation for a more precise determination of the nucleon form factors and also address all of the unsolved issues described in this paper. Such planning is now underway.

ACKNOWLEDGMENTS

We thank Toshimi Suda, Eigo Shintani and Oliver Bär for useful discussions, and Yusuke Namekawa for his careful reading of the manuscript. Numerical calculations for the present work have been carried out on the FX10 supercomputer system at Information Technology Center of the University of Tokyo, on the HA-PACS and COMA cluster systems under the “Interdisciplinary Computational Science Program” of Center for Computational Science at University of Tsukuba, on HOKUSAI GreatWave at Advanced Center for Computing and Communication of RIKEN, and on the computer facilities of the Research Institute for Information Technology of Kyushu University. This research used computa-

tional resources of the HPCI system provided by Information Technology Center of the University of Tokyo, Institute for Information Management and Communication of Kyoto University, the Information Technology Center of Nagoya University, and RIKEN Advanced Institute for Computational Science through the HPCI System Research Project (Project ID: hp120281, hp130023, hp140209, hp140155, hp150135, hp160125, hp170022, hp180072). We thank the colleagues in the PACS Collaboration for helpful discussions and providing us the code used in this work. This work is supported in part by MEXT SPIRE Field 5, and also by Grants-in-Aid for Scientific Research from the Ministry of Education, Culture, Sports, Science and Technology (No. 16H06002), and Grant-in-Aid for Scientific Research (C) (No. 18K03605).

* kuramasi@het.ph.tsukuba.ac.jp

† sasaki@nucl.phys.tohoku.ac.jp

‡ yamazaki@het.ph.tsukuba.ac.jp

§ RIKEN Advanced Institute for Computational Science (AICS) was renamed to RIKEN Center for Computational Science (R-CCS) in April 2018.

- [1] A. W. Thomas and W. Weise, *The Structure of the Nucleon*, Berlin, Germany: Wiley-VCH (2001) 389 p.
- [2] R. Pohl *et al.*, *Nature* **466**, 213 (2010).
- [3] R. Pohl, R. Gilman, G. A. Miller and K. Pachucki, *Ann. Rev. Nucl. Part. Sci.* **63**, 175 (2013).
- [4] M. Tanabashi *et al.* [ParticleDataGroup], *Phys. Rev. D* **98**, no. 3, 030001 (2018).
- [5] I. Sick, *Atoms* **6**, no. 1, 2 (2018).
- [6] A. Czarnecki, W. J. Marciano and A. Sirlin, *Phys. Rev. Lett.* **120**, no. 20, 202002 (2018).
- [7] C. C. Chang *et al.*, *Nature* **558**, no. 7708, 91 (2018).
- [8] T. Bhattacharya, V. Cirigliano, S. Cohen, R. Gupta, H. W. Lin and B. Yoon, *Phys. Rev. D* **94** (2016) no.5, 054508.
- [9] C. Alexandrou, M. Constantinou, K. Hadjiyiannakou, K. Jansen, C. Kallidonis, G. Koutsou and A. Vaquero Aviles-Casco, *Phys. Rev. D* **96**, no. 5, 054507 (2017).
- [10] R. Gupta, Y. C. Jang, B. Yoon, H. W. Lin, V. Cirigliano and T. Bhattacharya, *Phys. Rev. D* **98**, 034503 (2018).
- [11] J. R. Green, J. W. Negele, A. V. Pochinsky, S. N. Sritsyn, M. Engelhardt and S. Krieg, *Phys. Rev. D* **90**, 074507 (2014).
- [12] C. Alexandrou, M. Constantinou, K. Hadjiyiannakou, K. Jansen, C. Kallidonis, G. Koutsou and A. Vaquero Aviles-Casco, *Phys. Rev. D* **96**, no. 3, 034503 (2017).
- [13] K.-I. Ishikawa, N. Ishizuka, Y. Kuramashi, Y. Nakamura, Y. Namekawa, Y. Taniguchi, N. Ukita, T. Yamazaki and T. Yoshié [PACS Collaboration], *PoS LATTICE 2015*, 075 (2016).
- [14] T. Yamazaki, Y. Aoki, T. Blum, H.-W. Lin, M.-F. Lin, S. Ohta, S. Sasaki, R. J. Tweedie, and J. M. Zanotti [RBC+UKQCD Collaboration], *Phys. Rev. Lett.* **100**, 171602 (2008).
- [15] T. Yamazaki, Y. Aoki, T. Blum, H.-W. Lin, S. Ohta, S. Sasaki, R. J. Tweedie, and J. M. Zanotti [RBC+UKQCD Collaboration], *Phys. Rev. D* **79**, 114505 (2009).
- [16] B. Yoon *et al.*, *Phys. Rev. D* **95**, no. 7, 074508 (2017).
- [17] Y. Nambu and G. Jona-Lasinio, *Phys. Rev.* **122**, 345 (1961).
- [18] Y. Nambu and G. Jona-Lasinio, *Phys. Rev.* **124**, 246 (1961).
- [19] V. Bernard, L. Elouadrhiri and U. G. Meissner, *J. Phys. G* **28**, R1 (2002).
- [20] A. Bodek, S. Avvakumov, R. Bradford and H. S. Budd, *Eur. Phys. J. C* **53**, 349 (2008).
- [21] B. Bhattacharya, R. J. Hill and G. Paz, *Phys. Rev. D* **84**, 073006 (2011).
- [22] B. Bhattacharya, G. Paz and A. J. Troiano, *Phys. Rev. D* **92**, no. 11, 113011 (2015).
- [23] T. Goringe and H. W. Fearing, *Rev. Mod. Phys.* **76**, 31 (2003).
- [24] S. Choi *et al.*, *Phys. Rev. Lett.* **71**, 3927 (1993).
- [25] W. I. Weisberger, *Phys. Rev.* **143**, 1302 (1966).
- [26] S. Sasaki and T. Yamazaki, *Phys. Rev. D* **78**, 014510 (2008).
- [27] T. Bhattacharya, S. D. Cohen, R. Gupta, A. Joseph, H. W. Lin and B. Yoon, *Phys. Rev. D* **89**, no. 9, 094502 (2014).
- [28] S. Capitani *et al.*, *Phys. Rev. D* **92**, no. 5, 054511 (2015).
- [29] C. Alexandrou, M. Constantinou, S. Dinter, V. Drach, K. Jansen, C. Kallidonis and G. Koutsou, *Phys. Rev. D* **88**, no. 1, 014509 (2013).
- [30] S. Ohta [UKQCD and RBC Collaborations], arXiv:1710.06656 [hep-lat].
- [31] T. Yamazaki [PACS Collaboration], *PoS LATTICE 2015*, 081 (2016).
- [32] Y. Kuramashi, K.-I. Ishikawa, S. Sasaki, T. Yamazaki, N. Tsukamoto and A. Ukawa [PACS Collaboration], *PoS LATTICE 2016*, 158 (2016).
- [33] N. Tsukamoto, K.-I. Ishikawa, Y. Kuramashi, S. Sasaki and T. Yamazaki [PACS Collaboration], *EPJ Web Conf.* **175**, 06007 (2018).
- [34] Y. Iwasaki, preprint, UTHEP-118 (Dec. 1983), unpublished [arXiv:1111.7054 [hep-lat]].
- [35] C. Morningstar and M. J. Peardon, *Phys. Rev. D* **69**, 054501 (2004).
- [36] Y. Taniguchi, *PoS LATTICE 2012*, 236 (2012).
- [37] M. Lüscher, *JHEP* **0305**, 052 (2003).
- [38] M. Lüscher, *Comput. Phys. Commun.* **165**, 199 (2005).

- [39] M. Hasenbusch, Phys. Lett. B **519**, 177 (2001).
- [40] M. Hasenbusch and K. Jansen, Nucl. Phys. B **659**, 299 (2003).
- [41] P. de Forcrand and T. Takaishi, Nucl. Phys. Proc. Suppl. **53**, 968 (1997).
- [42] R. Frezzotti and K. Jansen, Phys. Lett. B **402**, 328 (1997).
- [43] R. Frezzotti and K. Jansen, Nucl. Phys. B **555**, 395 (1999).
- [44] R. Frezzotti and K. Jansen, Nucl. Phys. B **555**, 432 (1999).
- [45] S. Aoki *et al.* [JLQCD Collaboration], Phys. Rev. D **65**, 094507 (2002).
- [46] K.-I. Ishikawa, S. Aoki, T. Ishikawa, N. Ishizuka, K. Kanaya, Y. Kuramashi, M. Okawa, Y. Taniguchi, A. Ukawa and T. Yoshié [PACS-CS Collaboration], PoS LAT **2006**, 027 (2006).
- [47] P. de Forcrand, Nucl. Phys. Proc. Suppl. **73**, 822 (1999).
- [48] C. Alexandrou, P. de Forcrand, M. D’Elia and H. Panagopoulos, Phys. Rev. D **61**, 074503 (2000).
- [49] S. Sasaki, T. Blum and S. Ohta, Phys. Rev. D **65**, 074503 (2002).
- [50] K. Sasaki and S. Sasaki, Phys. Rev. D **72**, 034502 (2005).
- [51] G. Martinelli and C. T. Sachrajda, Nucl. Phys. B **316**, 355 (1989).
- [52] S. Sasaki, K. Orginos, S. Ohta, and T. Blum [RIKEN-BNL-Columbia-KEK Collaboration], Phys. Rev. D **68**, 054509 (2003).
- [53] K.-I. Ishikawa, N. Ishizuka, Y. Kuramashi, Y. Nakamura, Y. Taniguchi, N. Ukita, T. Yamazaki and T. Yoshié [PACS Collaboration], PoS LATTICE **2015**, 271 (2016).
- [54] T. Blum, T. Izubuchi and E. Shintani, Phys. Rev. D **88**, no. 9, 094503 (2013).
- [55] J. J. Kelly, Phys. Rev. C **70**, 068202 (2004).
- [56] C. G. Boyd, B. Grinstein and R. F. Lebed, Phys. Lett. B **353**, 306 (1995).
- [57] R. J. Hill and G. Paz, Phys. Rev. D **82**, 113005 (2010).
- [58] V. A. Andreev *et al.* [MuCap Collaboration], Phys. Rev. Lett. **99**, 032002 (2007).
- [59] V. A. Andreev *et al.* [MuCap Collaboration], Phys. Rev. Lett. **110**, no. 1, 012504 (2013).
- [60] R. J. Hill, P. Kammel, W. J. Marciano and A. Sirlin, Rept. Prog. Phys. **81**, no. 9, 096301 (2018).
- [61] R. Gupta, Y. C. Jang, H. W. Lin, B. Yoon and T. Bhattacharya, Phys. Rev. D **96**, no. 11, 114503 (2017).
- [62] O. Bär, arXiv:1808.08738 [hep-lat].
- [63] Y. Kuramashi, “A Large Scale Simulation of 2+1 Flavor Lattice QCD”, talk presented at 35th Internal Symposium on Lattice Field Theory (Lattice 2017), 18-24 June 2017, Granada, Spain.
- [64] K.-I. Ishikawa, N. Ishizuka, Y. Kuramashi, Y. Nakamura, Y. Namekawa, Y. Taniguchi, N. Ukawa, T. Yamazaki and T. Yoshié [PACS Collaboration], arXiv:1807.06237 [hep-lat].
- [65] After we complete this work, the new calculation method of the axial-vector coupling is developed based on the Feynman-Hellmann method in Ref. [7]. Their high-precision result is quite consistent with the experimental value.
- [66] There is some controversy about significant finite-volume effect when $m_\pi L \geq 4$ as reported in recent unquenched high-statistics calculations [7, 10, 16].
- [67] In a L^3 spatial box with periodic boundary conditions, one may consider that a half size of L corresponds to $2r_{\text{cut}}$.
- [68] The sign of all form factors is chosen to be positive. Remark that our γ_5 definition $\gamma_5 \equiv \gamma_1\gamma_2\gamma_3\gamma_4 = -\gamma_5^M$ has the opposite sign relative to that in the Minkowski convention ($\vec{\gamma}^M = i\vec{\gamma}$ and $\gamma_0^M = \gamma_4$) adopted in the particle data group [4].
- [69] For the proton, $G_E^p(0) = 1$ and $G_M^p(0) = \mu_p = +2.79285$, while $G_E^n(0) = 0$ and $G_M^n(0) = \mu_n = -1.91304$ for the neutron.
- [70] We use the singular value decomposition (SVD) algorithm to solve the least squares problem for high degree polynomials.
- [71] Recently, Ref. [60] claims that the error on the experimental value of 0.67(1) fm [19, 20] is underestimated because of the model dependent analysis using the dipole ansatz. Instead, the value of $\sqrt{\langle r_A^2 \rangle} = 0.67(13)$ fm is quoted in Ref. [60].